This is a preprint, the final version is subject to change, of the American Mineralogist (MSA)
Cite as Authors (Year) Title. American Mineralogist, in press.
(DOI will not work until issue is live.) DOI: http://dx.doi.org/10.2138/am-2017-6084

REVISION 3

Age discordance and mineralogy

Igor M. Villa[1,2], John M. Hanchar[3]

[1]Institut für Geologie, Universität Bern, Baltzerstrasse 3, 3012 Bern, Switzerland; igor@geo.unibe.ch

[2]Centro Universitario Datazioni e Archeometria, Università di Milano Bicocca,
piazza della Scienza 4, 20126 Milano, Italy

[3]Department of Earth Sciences, Memorial University of Newfoundland, 9 Arctic Ave., St John's, NL A1B 3X5
Canada; jhanchar@mun.ca

Abstract

Observations of discordant ages, meaning that an age given by one mineral geochronometer is different from the age given by another geochronometer from the same rock, began in the early days of geochronology. In the late 1950s and 1960s, discordant U-Pb zircon ages were unquestioningly attributed to Pb diffusion at high temperature. Later, the mineralogical properties and the petrogenesis of the zircon crystals being dated was recognized as a key factor in obtaining concordant U-Pb ages. Advances in analytical methods allowed the analysis of smaller and smaller zircon multigrain fractions, then the analysis of individual grains, and even pieces of grains, with higher degrees of concordancy. Further advances allowed a higher analytical precision, a clearer perception of accuracy, and a better statistical resolution of age discordance. As for understanding the cause(s) of discordance, belief revision followed the coupling of imaging, cathodoluminescence (CL) and back-scattered electrons (BSE), to in situ dating by secondary ion mass spectrometry (SIMS), or by laser ablation inductively coupled plasma mass spectrometry (LA-ICPMS). Discordant zircon and other accessory minerals (e.g.,

monazite, apatite, etc.) often consist of young rims accreted onto/into older cores. Age gradients are sharp, and no Pb diffusion gradients are observed. As U-Pb discordance in crystalline, non-radiation damaged grains is caused by diachronous, heterochemical mineral generations, interpretations of mineral ages, based on the exclusive role of diffusion, are superseded, and closure temperatures of zircon and monazite are irrelevant in geological reality.

Other isotopic systems (Rb-Sr, K-Ar) were believed, since the 1960s, to be similarly controlled by the diffusivity of radiogenic daughters. When zircon and monazite discordance were recognized as zone accretion/reaction with sharp boundaries that showed little or no high-temperature diffusive re-equilibration, the other chronometric systems were left behind, and interpretations of mineral ages based on the exclusive role of diffusion survived.

The evidence from textural-petrologic imaging (CL, BSE) and element mapping by electron probe microanalyzer (EPMA) or high spatial resolution SIMS or LA-ICPMS provides the decisive constraints. All microcline and mica geochronometers that have been characterized in detail document patchy textures and evidence for mineral replacement reactions. It is important not to confuse causes and effects; heterochemical microstructures are not the *cause* of Ar and Sr loss; rather, they *follow* it. Argon and Sr loss by dissolution of the older mineral generation occurs first, heterochemical textures form later, when the replacive assemblage recrystallizes. Heterochemical mineral generations are identified and dated by their Ca/Cl/K systematics in ^{39}Ar-^{40}Ar. Replacive reactions adding or removing Cl, such as, e.g., sericite overgrowths on K-feldspar, retrograde muscovite intergrowths with phengite, etc., are detected by Cl/K vs Ar/K isotope correlation diagrams. Calcium-poor reaction products, such as, e.g., young biotite intergrown with older amphibole, adularia replacing microcline, etc., can be easily identified by Ca/K vs Ar/K diagrams supported by EPMA analyses. Mixed mineral generations are observed to be the cause of discordant, staircase-shaped age spectra, while step-heating of crystals with age gradients produces concordant plateaus. Age gradients are therefore unrelated to staircase age spectra.

This is a preprint, the final version is subject to change, of the American Mineralogist (MSA)
Cite as Authors (Year) Title. American Mineralogist, in press.
(DOI will not work until issue is live.) DOI: http://dx.doi.org/10.2138/am-2017-6084

There is a profound analogy between the U-Pb, Rb-Sr, and K-Ar systems. Lead and Ar diffusion rates are both much slower than mineral replacement rates for all $T < 750$ °C. Patchy retrogression textures are always associated with heterochemical signatures (U/Th ratios, REE patterns, Ca/Cl/K ratios). As a rule, single-generation minerals with low amounts of radiation damage give concordant ages, whereas discordance is caused by mixtures of heterochemical, resolvably diachronous, mineral generations in petrologic disequilibrium. This can also include (sub-)grains that have accumulated significant amounts of radiation damage. For accurate geochronology the petrologic characterization with the appropriate technique(s) of the minerals to be dated, and the petrologic context at large, are as essential as the mass spectrometric analyses.

Introduction

A common observation of the early 1960s was that isotopic ages of different mineral chronometers from the same rock often gave discordant apparent ages, and therefore did not all record the crystallization of the mineral assemblage. Mineral ages of metamorphic rocks were often younger than the expected age of peak metamorphism. The reason for discordance of mineral ages between different dating methods, and within a single dating method, are the focus of the present paper.

Age determinations require an accurate solution of one equation, the age equation (Faure 1986), with two unknowns, t and F_0: $t = (1/\lambda) \times \ln(1 + (F(t) - F_0) / N(t))$, where t is the age, λ is the decay constant, $F(t)$ and $N(t)$ are the present-day concentrations of daughter and parent nuclides, respectively, and F_0 is the concentration of the non-radiogenic daughter isotope initially present in the crystallizing mineral. From a purely mathematical point of view, two samples having the same t and F_0, such as a pair of cogenetic minerals, are sufficient to uniquely constrain the two unknowns. In order to provide an internal consistency test, it is necessary to rely on overdetermination using four or more minerals

This is a preprint, the final version is subject to change, of the American Mineralogist (MSA)
Cite as Authors (Year) Title. American Mineralogist, in press.
(DOI will not work until issue is live.) DOI: http://dx.doi.org/10.2138/am-2017-6084

from the same rock to calculate a straight line (called an isochron; Faure 1986) that simultaneously solves for t and F_0. This allows a self-consistency check via statistical criteria (e.g., the chi squared test, or the MSWD parameter (mean square of the weighted deviates); McIntyre et al. 1966), which compares the purely statistical uncertainty with (geological or analytical) systematic artefacts. If MSWD > 1, the systematic bias of at least one of the data-points is greater than the random scatter.

Some minerals have a very high parent/daughter ratio, dictated by their respective partition coefficients. Methods for dating such minerals were thought to bypass the difficulty to identify, and measure, one or more cogenetic minerals that accurately constrain F_0, allowing an age calculation from a single mineral. This is done when the importance of the F_0 term in the age equation falls below a pre-set significance level; any systematic age bias due to inaccurate corrections for “initial Pb”, “Pb-loss”, "initial Sr", and "initial Ar" is therefore neglected.

Zircon has an extremely high U/Pb ratio, which makes it well suited for dating without finding a cogenetic mineral. Moreover, U has two long-lived radioactive isotopes. This allows to obtain two U-Pb ages from each measurement: the ^{235}U-^{207}Pb age, given by $t = (1/\lambda_{235}) \times \ln(1 + {}^{207}Pb^*/{}^{235}U)$, and the ^{238}U-^{206}Pb age, given by $t = (1/\lambda_{238}) \times \ln(1 + {}^{206}Pb^*/{}^{238}U)$. The asterisk denotes the radiogenic Pb, and λ_{238} and λ_{235} are the decay constant for ^{238}U and ^{235}U, respectively.

Early geochronological work on zircon showed that in some samples the ^{235}U-^{207}Pb age and the ^{238}U-^{206}Pb age agree, in some others they do not. The concordant samples are easily interpreted as ideal chronometers recording a geologically meaningful event (e.g. igneous crystallization), while the discordant samples evidently show deviations from ideal isotopic closure. To display U-Pb data and to explore ways to detect, and explain, discordance, Wetherill (1956) devised the so-called Concordia plot shown here in Fig. 1. The concordia curve is the geometric locus of all points whose two U-Pb ages are concordant.

This is a preprint, the final version is subject to change, of the American Mineralogist (MSA)
Cite as Authors (Year) Title. American Mineralogist, in press.
(DOI will not work until issue is live.) DOI: http://dx.doi.org/10.2138/am-2017-6084

99 The first working hypotheses that tried to explain the discordant U-Pb ages of zircon samples
100 (Tilton 1960; Wetherill 1963) assumed that age discordance was the effect of one single cause, Pb
101 being lost out of the zircon structure at high temperature by Fickian diffusion after the zircon
102 crystallized. Tilton (1960) calculated the frequency factor expressing Pb diffusion in zircon, $D/a^2 = 25$
103 $\times 10^{-12}$ $a^{-1} = 8 \times 10^{-19}$ s^{-1}. Wetherill (1963) quantified the prediction of a zircon's discordance by a very
104 sophisticated mathematical model as a function of Fickian diffusion of U and Pb in the zircon crystal
105 structure.

106 Dating single minerals is only apparently exempt of the necessity to first and foremost assess
107 petrological equilibrium and cogeneticity. Qualitative imaging by cathodoluminescence (CL) and/or
108 back-scattered electrons (BSE), and X-ray mapping, have increasingly made clear that mineral
109 chronometers are very seldom truly monomineralic. Quantitative proof is provided by compositional
110 characterization at the μm scale. Electron probe microanalysis (EPMA) routinely achieves this
111 resolution.

112 In the past few decades in situ microchemical analyses by laser ablation inductively coupled
113 plasma mass spectrometry (LA-ICPMS) achieved a modest spatial resolution of no better than a few
114 tens of μm. Recent work (e.g., Paul et al. 2012; Rittner and Müller 2012; Ubide et al. 2015; Zhou et al.
115 2017; Petrus et al. 2017; Chew et al. 2017) is pushing the resolution to <10 μm, for LA-ICPMS
116 mapping depending on the material analyzed and the elements/isotopes measured. Ion imaging and ion
117 tomography by secondary ion mass spectrometry (SIMS) can be done on terrestrial and other planetary
118 materials to produce ion maps and ion tomography images with a spatial resolution of ca. 2-3 μm (e.g.,
119 Kusiak et al. 2013, Nemchin et al. 2013; Whitehouse et al. 2014).

120 It is only fair to point out that the working hypotheses proposed by Tilton (1960) and Wetherill
121 (1963) were legitimate at the time, given the low-resolution analytical tools and laboratory procedures
122 that were then available. In fact, it is only thanks to improved imaging and in situ dating analytical

This is a preprint, the final version is subject to change, of the American Mineralogist (MSA)
Cite as Authors (Year) Title. American Mineralogist, in press.
(DOI will not work until issue is live.) DOI: http://dx.doi.org/10.2138/am-2017-6084

equipment that the relevance of volume diffusion in mineral geochronometers can be demonstrated on a case-by-case basis. Whether age discordance is due to thermally activated volume diffusion can be verified by a very simple, yet rigorous test. The concentration of the Fick's Law diffusant as a function of distance obeys a sigmoid curve (Crank 1975), called error function or erf(x), whereby the matrix remains inert by definition. Deviations of the diffusant concentration from the sigmoid gradient are mathematical proof that Fickian diffusion was not the only process causing the diffusant's mobility. Such deviations in mineral geochronometers are usually associated with patchy textures revealed by CL and/or BSE imaging. Patchy textures are typical of metasomatic alteration caused by infiltration of hydrothermal fluids leading to recrystallization of the original minerals (Villa and Williams 2013).

There are two possible explanations for intra-grain patchy age distributions. In the first interpretation, secondary structures are the *cause* of variable ages; replacive textures form first, followed by diffusion of radiogenic isotopes at a faster rate than in the primary mineral (because the grain size of the reaction products is smaller than that of the unreacted minerals). Thus, even systems recording recrystallization caused by fluids in a fault-plane are considered to preserve information on temperature-dependent diffusion (e.g., Arnaud and Eide 2000). In the second interpretation, the formation of secondary textures requires fluid circulation and coupled dissolution/reprecipitation (Putnis 2002, 2009; Williams et al. 2011; Putnis and Austrheim 2013). In this view, microstructural modifications are not the *cause* of isotope transport but *follow* it. Strictly speaking, both are actually two effects of one cause, namely dissolution/reprecipitation. However, dissolution occurs first, and is simultaneously accompanied by the loss of the radiogenic isotopes previously accumulated (such as Pb and Sr, which are incompatible in the structure of U-rich and of Rb-rich phases, respectively, and Ar, which is incompatible in all mineral structures). The new replacive patches form only later, when dissolution is followed by reprecipitation (Putnis and Austrheim 2013).

Dissolution/reprecipitation can manifest itself in several ways, all of which cause the crystallization of a new phase assemblage (Putnis and Austrheim 2013). Dissolution requires a reactive

This is a preprint, the final version is subject to change, of the American Mineralogist (MSA)
Cite as Authors (Year) Title. American Mineralogist, in press.
(DOI will not work until issue is live.) DOI: http://dx.doi.org/10.2138/am-2017-6084

fluid and is often accompanied by open-system exchange with the external environment. At near-surface temperatures, the recrystallization into a different phase assemblage is termed alteration. At higher P-T condition the terms metasomatism and metamorphism are used. On the atomic scale, all three phenomena are equivalent. The perception of metamorphic processes has shifted in the petrological community, leading to the consensus that all paragenetic changes, both prograde and retrograde, require fluids (Putnis 2009; Jamtveit 2010).

The quantitative comparison of the dissolution/reprecipitation rate with the diffusion rate of Pb and Ar in two widely used mineral geochronometers, presented in Figure 2, shows that at medium and low grade metamorphic conditions (for $T < 750$ °C, i.e., $1000/T > 0.98$), volume diffusion is the slower process by orders of magnitude. This very large difference in rates explains why intra-grain age variations are mostly observed in close association with patchy retrogression/recrystallization textures in metamorphic minerals, while observations of genuine erf(x)-shaped age gradients, required by diffusion mathematics, are rare exceptions (Villa and Williams 2013; Villa 2016, and references therein). In a grain featuring superposed diffusion and recrystallization (e.g., Labotka et al. 2004, their Fig. 4), the steepest gradient is the upper limit for diffusivity.

U-Pb geochronology is discussed in detail in the next section. $^{40}Ar/^{39}Ar$ (or, following the general use of indicating the parent-daughter pair in that order, ^{39}Ar-^{40}Ar) geochronology is discussed in detail in the section after that.

Age discordance in the U-Pb system

The diffusionistic interpretation of discordant U-Pb ages was undermined when *in situ* U-Pb geochronology by SIMS was combined with CL and BSE imaging (Gebauer et al. 1988; Paterson et al. 1989, 1992a, 1992b; Vavra 1990; Vavra and Hansen 1991; Hanchar and Miller 1993; Hanchar and Rudnick 1995). Imaging of zircon (and later monazite, apatite, xenotime, allanite, titanite, etc.) grains

This is a preprint, the final version is subject to change, of the American Mineralogist (MSA)
Cite as Authors (Year) Title. American Mineralogist, in press.
(DOI will not work until issue is live.) DOI: http://dx.doi.org/10.2138/am-2017-6084

using these techniques often revealed complex internal structures including growth (sometimes called oscillatory) and sectoral zoning, secondary zoning, inherited magmatic or metamorphic cores that are texturally distinct from subsequent magmatic or metamorphic overgrowths, etc. (e.g., Corfu et al. 2003) Prior to the introduction of those imaging methods, many of the internal features of the zircon were difficult, to impossible, to observe with conventional optical microscopy techniques.

Krogh and Davis (1975) improved the detection of the internal zircon structure by mounting grains in epoxy, polishing them to reveal the crystal interiors, etching them using HF acid vapour, and them imaging them using reflected light microscopy (or differential interference contrast microscopy, also known as Nomarski interference contrast or Nomarski microscopy) before analysis. For Proterozoic and Archean zircon, this procedure was quite effective in revealing internal zoning, cores, rims, etc., by preferentially etching the high U regions that had accumulated significant radiation damage. However, in Paleozoic, Mesozoic, and younger zircon, often there is not enough accumulated radiation damage to weaken the zircon structure enough to allow the HF vapour to effectively etch the zircon and therefore rendered this process ineffective in revealing the internal features of the zircon.

It is also frequently observed that inherited cores are not in the geometric center of the grain. If a simple sampling strategy was employed, where two analyses were done (one in the presumed core in the center and one in the presumed rim), it was often the case that the core was missed, or the core and rim were both analyzed with some proportion of each other in the analysis, or if the core was in fact close to the rim of the grain, it could appear that the grain had no overgrowth. In fact, some imaged microstructures and angular unconformities (such as zoning in the core truncated by a younger overgrowth) are clear evidence of multiple geologic events (Fig. 3). In the example in Figure 3, from a Cretaceous peraluminous granite (zircon rim region in Fig. 3) with a Proterozoic core (the darker regions in the asymmetrical center of the crystal), even with high resolution BSE imaging it is not obvious what the different regions in the zircon represent until they are dated by an appropriate technique. Analysis A is clearly in the rim and concordant, and analyses B, C, D, and E, are in the core

with analysis B the oldest region analyzed (and not obvious that should be the case based on the BSE image revealed internal structures). Analyses F and G could represent mixing of the core and rim ages, or be core ages that experienced Pb loss from the accumulation of radiation damage in the zircon structure. Note also that the core of this zircon grain is not in the geometric center of the crystal, and that there is an outer rim (dark in BSE) that was not analyzed.

Figures 4a and b are simplified illustrations of the different trajectories in the Wetherill (1956) Concordia diagram and the Tera-Wasserburg (1972a,b) Concordia diagram. Fig. 4 highlights where the different hypothetical analyses plot and why they plot where they do on each of the diagrams.

Within a decade of the first CL observations, the prevailing view regarding zircon geochronology was reformulated by Mezger and Krogstadt (1997); age discordance in zircon is now considered due to discrete events of open-system mass transfer, recorded by chemical heterogeneity (see also Corfu 2013). Microtextures such as growth zoning, fir tree zoning, sectoral zoning, bright/dark patches, etc. (Corfu et al. 2003) underline that corrosion, retrogression, recrystallization, and reprecipitation played an essential role and that the zircon matrix of such samples was neither homogeneous nor inert as required by Fick's Law for volume diffusion to be valid. Each textural zone in the zircon was reproducibly observed to be concordant by in situ dating whenever it had undergone minimal radiation damage and metamictization of the zircon structure from the decay of U and Th, and thereby had remained a closed system. Conclusive proof of the very low intrinsic diffusivity of Pb in zircon was provided by the laboratory measurements of Cherniak and Watson (2000). Möller et al. (2002) indeed observed that in a metamorphic zircon sample from Rogaland (Norway), the relict zones remain concordant despite undergoing UHT conditions (T > 950 °C). Nasdala et al. (2010) reported that extremely radiation damaged zircon crystals from the (Grenville age) Saranac Uranium Mine near Bancroft, Ontario, retained their primary U concentrations, with the implication that the U was immobile (but not Pb as many of their SIMS analyses were discordant), as revealed in EPMA X-ray maps (their Fig. 4), even though the crystals were essentially metamict. Deformation, if unaccompanied

by recrystallization promoted by an aqueous fluid, can achieve Pb mobility restricted to the scale below 1 μm (Piazolo et al. 2012, 2016).

One essential characteristic of all laboratory measurements of diffusivity is that they always represent a strict upper limit of the true diffusivity. It is possible (and sometimes likely, as in the case of the mica diffusivity experiments mentioned below) that unanticipated systematic biases affect the laboratory measurements. Such artefacts could pertain to the way that the concentration gradient is measured, or to the way that it is produced. If the calculation of the transport rate is not based on inverting an erf(x) profile (as documented, e.g., by Cherniak and Watson 2003) but on a bulk loss (as in Giletti 1974), there is no immediate proof that transport was due to a single process. If, moreover, the mineral being studied is heated in a sealed capsule containing free water, dissolution occurs, and the measured isotope distribution is controlled by the sum of two processes, diffusion and dissolution/reprecipitation (see, e.g., Villa and Puxeddu 1994; Dohmen et al. 1998, their Figs. 7a-h). In this case the rate of transport is greater than volume diffusion alone. An example of how to deconvolve the original Giletti (1974) data and to separate the dissolution rate in the capsule from true diffusivity was discussed by Villa (2010, p. 5).

Observations on the link between petrology and the isotope record have more recently been extended to monazite (e.g., Williams et al. 2007). The general consensus is growing that accurate ages require an accurate interpretation of petrogenesis, which in turn requires imaging by CL and/or BSE, and in the case of monazite BSE images and X-ray mapping using the EPMA, or element/isotope mapping by LA-ICPMS, or ion mapping or ion tomography imaging by SIMS. A given internal feature can be revealed by both CL and BSE imaging methods, whereby CL usually reveals more fine structure (Hanchar and Rudnick 1995; Corfu et al. 2003). Whenever metamorphic minerals are studied in sufficient detail, it becomes evident that few samples show constant (or simple bell-shaped) intra-grain age distributions.

In the very first paper introducing the Concordia diagram, Wetherill (1956) did not make an

explicit statement on the mechanism causing what he termed (incorrectly) "Pb loss" at high temperature. Radiogenic Pb (hereafter referred to as Pb*) was considered to be continuously or episodically lost from the zircon structure at high temperature during metamorphism or anatexis. In early studies, there was no discussion of the mineralogy of the zircon crystals analyzed. Moreover, in the 1960s there was a paucity of experimental data on volume diffusion in minerals. Therefore, the prevalent mathematical models of the early 1960s were based on the assumption that volume diffusion was more rapid than all other conceivable geologic processes. Phenomena unknown at that time include low-temperature Pb* loss due to metamictization of old and U-rich grains; incorporation of (otherwise incompatible) ^{204}Pb in minute heterochemical inclusions or along cracks or fractures; and, most importantly, complex mineralogical textures due to dissolution/reprecipitation such as metamorphic rims overgrowing inherited cores of a range of different ages. Therefore, such phenomena were not looked for, and therefore not observed.

Silver and Deutsch (1963) were the first to systematically consider the context between U-Pb geochronology and the mineralogical properties of zircon. That study followed a different approach than the earlier studies of Weatherill and Tilton, and instead of using elaborate mathematical models to explain the diffusive behavior of Pb*, they tried to empirically understand the properties of zircon. Silver and Deutsch found that the multigrain zircon fractions they studied, separated from a 100 kg granodiorite block, showed heterogeneous U-Pb systematics. They compared the U-Pb data with parameters such as morphology, zoning (in transmitted light and mounted in epoxy and polished to reveal the crystal interiors – not using CL or BSE, as they were unavailable at that time), color, inclusions, size distribution, radioactivity, refractive index, unit cell dimensions, and magnetic properties.

Present-day in situ studies of individual grains from samples with similar complex mineralogy document a correlation between petrology and isotope systematics (e.g., Villa and Williams 2013, and references therein). Silver and Deutsch (1963) also proposed that zircon started to crystallize early in

the history of the melt and continued to grow over most of the crystallization history. The residual liquid was enriched in incompatible elements, including U and Th, and as a result late crystallizing zircon (i.e., either whole magmatic zircon crystals or magmatic rims on inherited cores) was enriched in those elements and therefore was more affected by the effects of metamictization caused by the radioactive decay of U and Th. They also raised the question of the effects on the U-Pb systematics of metasomatic alteration of zircon by hydrothermal fluids.

The next major breakthrough in understanding and minimizing the effects of discordance was achieved a decade later by Krogh, and published in Carnegie Institution of Washington Yearbooks (Krogh 1970, 1971) and journal articles. Krogh (1973) presented a low Pb background dissolution method for the hydrothermal dissolution of zircon. By improving the laboratory contamination in the dissolution procedure, researchers could analyze smaller fractions of zircon (e.g., < 1 mg) which in turn led to improvements that eventually led to the analysis of individual zircon grains and even pieces of zircon (e.g., Steiger et al. 1993) and monazite (e.g., Hawkins and Bowring 1997). The possibility to analyze single zircon grains, and pieces of grains, allows researchers to select well-characterized, high quality, crystals and to contrast the results obtained from them with the less precise and more discordant results obtained from lower quality individual grains from the same rock. It also provides a clear distinction between xenocrysts (inherited crystals formed in a different magma chamber during a previous magmatic episode and passively entrained by the current erupting magma); antecrysts (crystals grown early in the history of the magma, when the magma chamber responsible for the current eruption/intrusion started its maturation); and last-generation autocrysts (crystals still growing at the very end of the current magmatic episode, at the time of eruption/intrusion) (Miller et al. 2007; Schoene et al. 2010).

In two subsequent papers, Krogh (1982a, b) presented an improved method for paramagnetic separation and a method for using air to abrade zircon grains. This methodology eliminated 90-100 % of discordance and improved the precision of the analyses to ± 1-3 Ma for zircon grains with an age of

2700 Ma. The air abrasion technique preferentially removed the U-rich outer layers of the zircon crystals, because they are weaker due to the higher U contents, which results in accumulation of radiation damage and subsequent metamictization of the zircon crystals. As those regions are also more susceptible to cracking and thus to ingress of ^{204}Pb carried by external fluids, Krogh's method achieved a removal of as much as 80 % of the ^{204}Pb present in the zircon crystals.

A further development in the same direction was termed chemical abrasion thermal ionization mass spectrometry (CA-TIMS) by Mattinson (2005). This method endeavors to remove the high U radiation-damaged, and thus more soluble, regions in zircon using high-temperature annealing (typically ca. 900-1000 °C for 48-60 hours followed by leaching in concentrated HF for a few hours at c. 190°C (Mundil et al. 2004). If followed by stepwise leaching, the method allows an easy recognition of Pb loss due to interaction of damaged crystals with low-temperature fluids and often leads to the formation of a geologically meaningful "age plateau" (Mattinson 2011, Huyskens et al. 2016).

Depth profiling is an analytical approach sometimes used to study intra-grain age distributions in order to allow diffusion modelling of core-rim age differences, and to analyze thin rims (5-10 μm) on accessory minerals that otherwise cannot be analyzed once the grains are mounted in epoxy and polished to reveal the crystal centers. Due to the generally low number of radiogenic nuclides to be counted, geochronological depth profiling needs larger and deeper sampling volumes than element profiling in geochemical investigations and in diffusion experiments. As pointed out by Villa (2016), sub-µm spatial resolutions are required to positively identify genuine intra-grain diffusion profiles from discrete, diachronous mineral generations. Also, the concept of depth profiling the outside rim of a zircon is in conflict to what Krogh (1982a, b) proposed; that by removing the outer high-U regions in zircon by air abrasion, the resulting zircon showed less dispersion and was more concordant by removing any ^{204}Pb at the surface (in cracks, fractures, etc.), and regions that had experienced Pb loss through the radiation damage produced in the high-U regions. A serious problem with depth profiling is that it cannot be associated with CL/BSE imaging. This forfeits any information on the identity of the

phases analyzed and disables constraints on the petrogenetic mechanisms involved in their genesis. Neglecting the petrological characterization of samples led Grove and Harrison (1999) to model rim-core age increases in monazite grains solely as an invertible function of temperature, despite the recognition that monazite grains are predominantly comprised of heterochemical and diachronous patches, whereby zones near the rim can, but need not, be the youngest (DeWolf et al. 1993; Cocherie et al. 1998; Fisher et al. 2017). A useful indicator would be the examination of multi-element profiles (Villa 2016, his Fig. 2b). As the respective diffusivities of ions having different radii and charges are expected to be unrelated to the fluid/mineral partition coefficients, even without CL/BSE imaging it is straightforward to discriminate whether the cause of age discordance is Pb* loss (compatible with smooth multi-element diffusion profiles) or accretion of diachronous and heterochemical mineral generations (identified by patchy, non-monotonic profiles).

There appears to be a critical length-scale below which the concept of concordance can no longer be defined in a meaningful way. The combination of U-Pb geochronology with CL/BSE images obtained with (sub-)µm resolution (Kusiak et al. 2013; Valley et al. 2014) reveals that two processes occur at the nm scale: firstly, the recoil of intermediate decay-product nuclides and of associated α particles creates extended defects and at the same time removes the daughter nuclide from the crystallographic location of its parent; and secondly, high-temperature diffusion of Pb* by a few nm (which is irrelevant for the geochronology of grains > 100 µm and therefore usually not considered (Mezger and Krogstadt 1997)) concentrates the interstitial Pb* ions (and Y ions (Valley et al. 2014)) into traps corresponding to radiation-created extended defects. Such closed-system redistribution was observed (Kusiak et al. 2013; Valley et al. 2014) to disproportionate the Pb*/U ratio locally by increasing it in the Pb* traps and lowering it in the recoil-depleted source areas. The paradox conclusion is that a single-grain TIMS analysis of zircon that underwent high-temperature metamorphism or anatexis gives a perfectly concordant, undisturbed U-Pb age, but atom-probe analyses of the same grain at a scale < 1 µm can give both positively and negatively discordant "single-

This is a preprint, the final version is subject to change, of the American Mineralogist (MSA)
Cite as Authors (Year) Title. American Mineralogist, in press.
(DOI will not work until issue is live.) DOI: http://dx.doi.org/10.2138/am-2017-6084

348 atom" ages. It is only the whole-grain average at the 100 μm scale that balances out the nm-scale
349 heterogeneities and results in a concordant age.

350 A similar small-scale disproportionation had been reported by McLaren et al. (1994), albeit
351 with a slightly lower resolution approach (that was appropriate for the time when this study was done)
352 in their investigation of reverse discordance in in situ SIMS U-Pb analyses of zircon. In that study,
353 McLaren et al. found that microstructural features identified in a high U Sri Lankan zircon crystal,
354 using transmission electron microscopy (TEM), could be related to the reversely discordant U-Pb ages.
355 Those authors suggested that in the high U metamict regions, the U is decoupled from the Pb; with the
356 U being partitioned into the zirconia (tetragonal ZrO_2), and the Pb partitioned into the amorphous
357 "silica glass" phase. The zirconia and amorphous silica glass are produced when zircon incongruently
358 breaks down through the metamictization process (e.g., Ellsworth et al. 1994). The glass phase
359 preferentially sputters during the SIMS analysis leading to an apparent excess of radiogenic Pb and
360 producing the observed reverse discordance (McLaren et al. 1994)

361 Another very widely diffused U-Pb and Th-Pb mineral chronometer is monazite, which also is a
362 thermally very retentive mineral chronometer. Monazite is also known to not incorporate significant
363 amounts of ^{204}Pb when it crystallizes (Parrish 1990) making it a suitable target for U-Pb
364 geochronology. It is well known (e.g., Bingen and van Breemen, 1998) that temperatures around 800-
365 850 °C leave the U-Pb age of monazite unaffected. On the other hand, it is also well established that
366 mass transfer during chemical open-system events promotes patchy recrystallization, and
367 corresponding age rejuvenation, at much lower temperatures (Williams et al. 2007, 2011; Laurent et al.
368 2016). The abundant imaging data reported in the literature (including BSE images and EPMA X-ray
369 and maps), demonstrating very widespread intra-grain genetic heterogeneities, have brought about an
370 abandonment of bulk-grain analyses. Analyzing a polygenetic grain, which is very retentive of its
371 radiogenic Pb, is easily predicted to give rise to a discordant data-point.

372 The analytical approach most established in the literature is in situ dating, either by LA-ICPMS

(Paquette and Tiepolo 2007; Gregory et al., 2009; Goudie et al. 2014), SIMS (Stern and Bergman, 2001; Fisher et al. 2017), or EPMA (Williams et al. 2007). In the case of monazite, however, BSE imaging is often less effective than X-ray maps to reveal the internal structures of monazite crystals (Williams et al. 2011; Fisher et al. 2017). As (multiply) zoned monazite grains are the rule rather than the exception, it would be natural to expect that most studies, even those doing single-grain analyses, would report a great deal of discordant data-points. However, in contrast to zircon, the interpretive paradigm of monazite data evolved away from a description of discordance and towards exploring the tight links between petrology, microchemistry, and in situ geochronology. As the present paper deals with discordance, monazite offers much less pertinent, and less abundant literature than zircon. The analytical protocols just mentioned make discordant data-points very rare, as intra-grain zones, once they are formed, are extremely unlikely to ever lose Pb*. The most important rejuvenation mechanisms for monazite are coupled dissolution and reprecipitation (i.e., recrystallization: Putnis 2009), which once either process occurs, removes an entire (sub-)grain but causes no discordance in any of the surviving (sub-)grains (e.g., Parrish 1990; Hawkins and Bowring 1997; Macfarlane et al. 1997; Harlov et al. 2007; Hetherington and Harlov 2008; Harlov and Hetherington 2010; Harlov et al. 2011; Williams et al. 2011; Goudie et al. 2014; Fisher et al. 2017).

In addition to zircon and monazite, several more mineral chronometers are currently used with the U-Pb method, among which are apatite, titanite, and rutile. For all three minerals, there are reliable diffusivity data (Cherniak et al. 1991; Cherniak 1993; 2000; 2010). As in all three cases the diffusion coefficients at temperatures typical of mid-crustal metamorphism are orders of magnitude higher than for zircon, it could be expected that discordance by Pb loss (Tilton, 1960) would be observed very often. Instead, only a small number of papers report discordant apatite, titanite, or rutile (e.g., Romer 1996; Corfu and Stone 1998; Bracciali et al. 2013).

Discordance of apatite in the samples studied by Romer (1996) occurred below 150 °C and was attributed by him to incomplete hydrothermal recrystallizazion. Romer (1996) also reported observing

two discrete apatite generations; late overgrowths that were separated from the older cores by a corroded grain surface. The apatite and titanite analyses reported by Corfu and Stone (1998) are indistinguishable from concordia in most samples. As titanite occurs in two clearly distinct hetero-chemical generations in the samples studied, Corfu and Stone (1998) proposed local fluid activity as a likely event affecting some, but not all, of their samples and effecting a complete resetting of apatite, titanite, and rutile (as well as causing anomalous Sr isotopic compositions reported in the preceding literature). Such an open-system fluid circulation would also explain why only two apatite samples lie resolvably below concordia whereas at least 25 % of the apatite samples lie reversely discordant above concordia due to U loss and/or Pb addition. Note that, in this (rather unusual) instance, the natural fluid circulation caused the same chemical fractionation in the studied apatite samples as the laboratory artefact attributed to microbeam analyses in Fig. 4a.

Discordance of rutile, on the other hand, is attributed by Bracciali et al. (2013) to the incorporation of nonradiogenic Pb (monitored by ^{204}Pb). In the detrital samples that they analyzed, the petrogenetic context is no longer visible and speculations on the mechanisms causing discordance are not possible.

The case of rutile resulted in an apparent paradox. Kooijman et al. (2010) reported age gradients in natural rutile crystals obtained by LA-ICPMS, and calculated a higher diffusivity than that measured in the laboratory experiments by Cherniak (2000). As Fick's Law of diffusion is the slowest transport mechanism in most metamorphic environments (Fig. 2), two cases of inequality can occur: (A) the transport rate measured in the laboratory is faster than that estimated basing on non-isotopic constraints in natural samples, and (B) the transport rate in natural samples is faster than in the laboratory.

Case (A) is verified in sealed-capsule experiments whose reactants include free water (Villa 2010). In these experiments, the transport rate is the sum of a large term, the dissolution rate, and a smaller one, Fick's Law diffusivity. The smallest among all rate estimates is the closest one to the pure diffusivity. Case (B) cannot be due to laboratory artefacts of some kind of "stifled transport", as it is

423 impossible to fix atoms and prevent them from diffusing as T increases. Diffusion occurs in any case in
424 all systems. As in the preceding case, the lowermost transport rate is closest to the true diffusion rate;
425 higher transport rates necessarily derive from a sum of (unaccounted) processes. The spatial resolution
426 of the Kooijman et al. (2010) measurements was limited by the laser pit size, 35 μm diameter by 40 –
427 45 μm depth, i.e., a much longer length scale than the distance of the measurement points in the
428 Cherniak (2000) experiments. This provided Kooijman et al. (2010) a less certain documentation of an
429 erf(x) diffusion profile. As discussed by Villa (2016, his Fig. 2), a diffusive erf(x) profile necessarily
430 affects all atomic species of the mineral, not just the radiogenic isotopes. If at least one major or trace
431 element displays a patchy gradient, or if the element ratio trends antithetically to the prediction of the
432 ionic radius and charge systematics, it means that the interpolation of the observed daughter/parent
433 profile by the erf(x) function is inaccurate. Kooijman et al. (2010) only reported the Pb*/U ratio, and
434 the evidence of partial recrystallization as the cause of the anomalously fast Pb* transport in rutile
435 remains circumstantial.
436
437 **Age discordance in the Rb-Sr and K-Ar systems**
438
439 Other isotopic systems yield discordant age data even more often than the U-Pb chronometers.
440 In a paper long considered a classic, Hart (1964) described massive, ubiquitous rejuvenation of Rb-Sr
441 and K-Ar mineral chronometers of Proterozoic country rocks from the contact aureole associated with
442 the Eocene Eldora (Colorado) pluton. The aureole minerals analyzed gave Rb-Sr and K-Ar ages that
443 varied from sample to sample; no mineral chronometer gave the same age as the others in the same
444 rock. Hart (1964) extrapolated the concept of diffusive Pb loss from zircon to Sr and Ar loss from the
445 aureole minerals, attributing the discordance to thermally driven volume diffusion in an otherwise
446 chemically closed mineral-rock system. We will argue instead that metasomatism, caused by

447 infiltration of hydrothermal fluids in the contact aureole-pluton system, was orders of magnitude more
448 important in causing these age disturbances.

449 Skarns and contact aureoles feature replacive low-*P*, high-*T* mineral assemblages. It is a self-
450 evident consequence of Lavoisier's mass conservation law that secondary assemblages require a
451 chemically open system and fluid-associated mass transfer. As an example, porphyry copper
452 mineralization occurs near the apex of intrusive bodies because the fluids, exsolved from the granite,
453 transported chalcophile elements, not because heat creates Cu. Hart (1964) indeed described retrograde
454 reactions and mass transfer in the Eldora contact aureole, but preferred to attribute the loss of Ar and Sr
455 to pure Fick's Law thermal diffusion in a chemically inert matrix. From the rejuvenation of K-Ar and
456 Rb-Sr ages, he calculated diffusion coefficients for biotite. A re-examination of Hart's (1964) original
457 data allows a reassessment of the validity of his conclusions.

458 Hart's (1964) interpretations, as originally presented, contain a physically incorrect calculation,
459 as his samples had undergone a significant size reduction during contact metamorphism (which in itself
460 is an indication of recrystallization). He was comparing the Ar loss rate, D/a^2, for large biotite grains
461 away from the contact with that for small grains near the contact. This created an artifact by decreasing
462 the true diffusion coefficient D of the samples furthest from the contact, as one order of magnitude
463 decrease in D/a^2 is accounted for by the factor of 3.1 in their grain size. Thus, the slope of the
464 Arrhenius diagram as used by Hart (1964, his Fig. 8) overestimates the activation energy of the process
465 responsible for Ar loss in biotite. Moreover, Hart was assuming diffusion from a sphere, while
466 subsequent work (Giletti 1974) utilized a more physically realistic cylindrical geometry. From the raw
467 data provided by Hart (1964, Table 2), it is necessary first to transform the calculated D/a^2 into
468 cylindrical D, and then divide D by one single grain radius common to all samples, taken here as a =
469 100 μm to make results directly comparable to those by Giletti (1974) discussed below. The D_0/a^2 and
470 E as originally proposed (5×10^{-7} s^{-1} and 23 kcal/mol, respectively), together with the correctly
471 recalculated D_0/a^2 and E (5×10^{-8} s^{-1} and 19 kcal/mol, respectively), are plotted in Figure 2.

Dodson (1973) systematized the diffusionist approach in a mathematical definition of the concept of "closure temperature" T_c for the retention of Ar, Sr, Pb, etc. As an example, the "closure temperature" of a 100 μm radius phlogopite grain cooling at 20 °C/Ma can be calculated from E and D_0/a^2 proposed by Hart (1964) as T_c = 254 °C. The closure temperature would be a useful concept if the retention of radiogenic isotopes depended solely on T and volume diffusion, as is the case for retention of fission tracks and He in apatite. In this case, it would be possible to constrain cooling histories and, to the extent that the paleo-geothermal gradient is accurately known, provide a proxy for exhumation. However, both the activation energy and the "closure temperature" of phlogopite calculated from Hart's estimates are in gross contrast with the diffusion experiments by Giletti (1974). The question arises why the Eldora "natural laboratory" came to be so discrepant from the controlled experimental laboratory conditions.

The qualitative petrological argument that geological processes in contact aureoles are principally controlled by fluids can be quantified by means of the dissolution rates measured by Wood and Walther (1983). Several other studies quantified the dissolution rates of minerals in near-surface conditions and soils. Wood and Walther (1983) determined the silicate dissolution rates over a broad interval at high T, thus estimating an activation energy. It is an essential part of this discussion that the fast dissolution rate proposed by Wood and Walther (1983) still stands as a lower limit, as no subsequent studies (e.g., Gruber et al. 2016) have revised it downwards. Figure 2 quantitatively compares the relative importance of Ar loss by volume diffusion and by dissolution/reprecipitation in the founding example of diffusionism. The rate of Ar loss from biotite from the Eldora aureole (corrected after Hart 1964) is shown in Figure 2 together with the dissolution rate measured by Wood and Walther (1983), the diffusivity of Pb in apatite (Cherniak et al. 1991), and the nominal Ar diffusivity inferred from the measurements by Giletti (1974). Villa (2010) corrected the Giletti (1974) results for systematic deviations from Fick's Law, probably due to partial dissolution caused by the presence of liquid H_2O in the capsule. This correction is validated by its agreement with the later

This is a preprint, the final version is subject to change, of the American Mineralogist (MSA)
Cite as Authors (Year) Title. American Mineralogist, in press.
(DOI will not work until issue is live.) DOI: http://dx.doi.org/10.2138/am-2017-6084

497 experiment by Giletti and Tullis (1977), which was done in absence of liquid water. The Eldora
498 samples all lie above the nominal Ar diffusivity, defining the same slope as the silicate dissolution line.
499 The Eldora and the phlogopite regression lines intersect at x = 1.180 (T = 574 °C). At 300 °C (x =
500 1.745) the laboratory diffusivity is 6.5 orders of magnitude slower than the Ar loss rate in the field.
501 This rounds off the proof that the mechanism causing the biotite age trend in the Eldora aureole was not
502 heat conduction leading to volume diffusion during the contact metamorphic event, but rather fluid-
503 induced recrystallization, as the latter is a faster process by several orders of magnitude.

504 Muscovite has always been considered the most retentive of the micas (Jäger 1967). Its
505 chronometric behaviour is crucial for understanding K-Ar systematics at large. Field evidence for the
506 very low intrinsic Ar diffusivity in muscovite is provided by the evidence of multiple white mica
507 generations with resolvably different ages in the same sample (Villa et al. 2014) and by the comparison
508 of U-Pb ages of monazite and K-Ar ages of muscovite in a metamorphic terrain infiltrated by aqueous
509 fluids (Tartèse et al. 2011). The latter authors documented a tight parallelism between these two
510 mineral chronometers, which implies that the loss of Pb* and Ar is controlled by the same mechanism.

511 Thus, thermally activated diffusion falls far short of causing discordance not only in the U-Pb
512 system but also in the K-Ar and Rb-Sr systems. In order to understand the true cause of the discordance
513 of K-Ar and Rb-Sr mineral chronometers, it is necessary to scrutinize what these dating methods are
514 based on.

515 Rb-Sr is mainly a “bulk sample” technique, by which the intra-grain isotope distribution is
516 usually not measured. This limits the information on causes and extent of discordance relative to, for
517 example, U-Pb dating of zircon and monazite samples. Even so, it is possible to detect discordance by
518 using overdetermined isochrons on a large number (n >> 2) of minerals from the same rock. The
519 isochron calculation yields the MSWD parameter (McIntyre et al. 1966). If MSWD >> 1, then the
520 sample is unlikely to ever have been in isotopic equilibrium. By linking the petrological information on
521 relict versus neoformed mineral phases to the Rb-Sr systematics, it is possible to unravel the system's

This is a preprint, the final version is subject to change, of the American Mineralogist (MSA)
Cite as Authors (Year) Title. American Mineralogist, in press.
(DOI will not work until issue is live.) DOI: http://dx.doi.org/10.2138/am-2017-6084

522 discordance (e.g. Glodny et al. 2008). Neoformed phases define a low-MSWD isochron, whereas the
523 petrologic relicts that carry Sr isotopic inheritance deviate from this isochron. A regression of relict
524 phases together with the neoformed phases gives an unacceptably high MSWD, due to a lack of
525 cogeneticity and of initial isotopic equilibrium. In case detailed petrologic groundwork evidences that a
526 given rock contains more than one mineral generation (be it retrogressive or relict phases in addition to
527 the magmatic or metamorphic assemblage), the whole rock data-point should never be used for an
528 internal isochron, as it cannot be in isotopic equilibrium with any of its heterogeneous constituents.

529 Before a detailed discussion of the K-Ar decay system (and its present-day analytical variety by
530 irradiation with fast neutrons, referred to here as ^{39}Ar-^{40}Ar), it will be beneficial to briefly recall the
531 features that characterized the ^{39}Ar-^{40}Ar dating technique at the time of its first development. In the
532 1960s, the Berkeley group around physicist John Reynolds developed the I-Xe dating method by
533 stepwise heating of irradiated samples (Jeffery and Reynolds 1961). Reynolds (1963) used three-
534 isotope common-denominator correlation diagrams to identify Xe derived from ^{129}I and ^{244}Pu, together
535 with its carrier phases. A spin-off of I-Xe, a combination of trace-element determinations and K-Ar
536 dating, was proposed by Merrihue (1965). This approach was pursued by Merrihue and Turner (1966),
537 who displayed their data with correlation diagrams. The dating method later came to be called
538 ^{40}Ar/^{39}Ar by Mitchell (1968), who also devised the age spectrum diagram. This data presentation was
539 perceived as a more immediate type of visualization and became very successful. The shift from
540 isotope correlation diagrams to age spectra puts all emphasis on a single isotope, ^{39}Ar. As graphics
541 limit how much we extract from data, this simplified presentation curtailed Merrihue's (1965)
542 discovery that rare gas isotopes (9 for Xe, 6 for Kr, 5 for Ar) in irradiated samples reveal
543 concentrations and carrier phases of trace elements such as U, I, Ba, Br, Cl, Ca, and K.

544 Turner et al. (1971) endeavored to date a lunar basalt using the ^{39}Ar-^{40}Ar method. Because of
545 severe sample size limitations, their first analysis was done on an untreated whole-rock chip, which
546 returned a markedly discordant age spectrum. Turner et al. (1971) went on to enrich a plagioclase by

handpicking and obtained an age spectrum with a greatly reduced discordance (Fig. 5a). In an interpretive scheme based exclusively on the age spectrum it is difficult to pinpoint the cause of the reduction of the age discordance by handpicking. Information is lost irretrievably if just the two isotopes $^{40}Ar^*$ and ^{39}Ar are considered. Only the full inventory of isotopes allows the recognition and simultaneous dating of carrier phases. This was done by Turner et al. (1971) by linking the Ca/K signature of the released Ar to plagioclase, groundmass matrix (termed mesostasis by Turner et al. 1971), and pyroxene. An alternative presentation of the same data in a common denominator three-isotope correlation diagram is presented here in Fig. 5b.

Few studies (e.g., Onstott et al. 1991) extrapolated to terrestrial samples the approach by Turner et al. (1971) that identifies mineral mixtures by heterogeneities in the $^{38}Ar/^{39}Ar$ and $^{37}Ar/^{39}Ar$ ratios. In most other terrestrial geology studies it was rarely taken into account that carrier phases that have not been completely reequilibrated by diffusion usually yield different mineral ages. The potential of ^{38}Ar and ^{37}Ar to fingerprint the chemically heterogeneous mineral generations is not exploited by age spectra, but only by multi-element-based three-isotope correlation diagrams. In fact, ever since the work by Reynolds (1963) and Turner (1965), it is clear that the halogen-derived ^{128}Xe and ^{38}Ar are essential for the detection of heterochemical phases. Moreover, such phase inventories can nowadays be identified with imaging techniques such as CL, BSE, and X-ray element maps, and quantified by EPMA in situ chemical analyses. Their identification by EPMA in combination with common denominator Ar isotope correlation diagrams, and their association with discordant age spectra, forces the conclusion that discordance in K-Ar, just as in U-Pb and I-Xe, is due to mixed mineral generations (e.g. primary crystallization and later metasomatic alteration zones or regions, produced by the infiltration of hydrothermal fluids).

Figure 6 highlights that CL imaging (Figs. 6a, c, e) can offer additional petrological information with respect to optical microscopy (Figs. 6b, d, f). In Figure 6a, the dark regions of the K-feldspar (sanidine) crystals have been partially dissolved and replaced by melt but the crystals have a “fresh”

572 igneous CL emission. In Figure 6c the K-feldspar (microcline) crystal has been partially
573 hydrothermally altered and replaced by low-temperature, non-luminescing adularia (Chafe et al. 2014).
574 In Figure 6e, the green CL plagioclase (albite) shows some alteration and a "core" that is enriched in
575 Ba and Sr (that is not visible in the cross-polarized photograph in Fig. 6f). The blue CL K-feldspar also
576 shows some hydrothermal alteration and partial replacement by adularia.

577 Indeed, monomineralic samples give concordant age spectra even if they feature intracrystalline
578 age gradients (Hodges et al. 1994). It can be noted that the patchy, asymmetric intracrystalline age
579 distributions in the samples documented by Hodges et al. (1994), as was the case with that reported by
580 Phillips and Onstott (1988), are incompatible with true volume diffusion, as the erf(x) function is
581 symmetrical and has its maximum at the center of the grain. Polymineralic samples, formed by mixed
582 mineral generations, are typical in retrogressed rocks, in which replacement reactions resulted in
583 petrologic disequilibrium unaccompanied by diffusive re-equilibration. EPMA X-ray element maps can
584 quantify their characteristic patchy textures. Mineral chronometers (micas, amphiboles, K-feldspar)
585 showing secondary reactions also show Ca/Cl/K signatures that correlate with step ages (e.g., Chafe et
586 al. 2014). Correlation plots linked to EPMA successfully unravel ages of each mineral generation (e.g.,
587 Villa et al. 2000). The recognition that Ca/K and Cl/K ratios can identify the end-members of a phase
588 mixture led to the definition of "isochemical steps" (Müller et al. 2002; Villa et al. 2006) as those steps
589 that have a uniform Ca/Cl/K signature. As it was observed that isochemical steps usually have uniform
590 ages as well, the implication is that isochemical steps monitor the degassing of one isochemical phase
591 characterized by a (nearly) concordant age, the "isochemical age".

592 As a working hypothesis, it can be stated that the coincidence between discordant ^{39}Ar-^{40}Ar age
593 spectra and the presence of heterochemical, diachronous, mineral phases is not a mere occasional
594 coincidence but a causal necessity. In order to test this hypothesis, three steps are required:

This is a preprint, the final version is subject to change, of the American Mineralogist (MSA)
Cite as Authors (Year) Title. American Mineralogist, in press.
(DOI will not work until issue is live.) DOI: http://dx.doi.org/10.2138/am-2017-6084

595 (A) Artificially create a mixture of heterochemical, diachronous minerals and examine: (A1) if
596 a discordant age spectrum is produced and (A2) if the age signature of the mixed minerals can be
597 unravelled by the appropriate three-isotope correlation diagrams.
598 (B) Identify natural heterochemical systems, for which sufficiently large grains allow the
599 mapping of intra-grain age gradients and compositional mapping, and compare them to the artificial
600 mixtures.
601 (C) Identify natural monomineralic systems, for which intra-grain K-Ar age gradients both
602 follow the bell-shaped erf(x) profile required by Fick's Law for an inert, unreacted matrix, and are in no
603 way associated with chemical heterogeneities, and compare them with the mixtures described in (A)
604 and (B).
605 An artificial mixture following (A) was first described by Wijbrans and McDougall (1986), who
606 reported that a mixture between a young muscovite and an older phengite, both of which gave
607 comparatively flat spectra, yielded a discordant, hump-shaped age spectrum. As these authors provided
608 an incomplete dataset (no ^{37}Ar or ^{38}Ar were determined), the potential of the experiment was not fully
609 exploited. Subsequent artificial mixtures were reported by Villa et al. (1996) and by Kula et al. (2010).
610 Villa et al. (1996) observed unexpected differences between step-heating and step-leaching age spectra
611 of a natural hornblende separate. By TEM they detected secondary K-feldspar in a cleavage from an
612 amphibole grain. This led to the hypothesis that the distinct differential degassing rate was the signature
613 of a secondary phase. To test this hypothesis, they mixed young K-feldspar with the older amphibole.
614 The age spectrum of the mixture offers no immediately obvious clarification (Fig. 7a). However,
615 unravelling is provided by exploiting all five Ar isotopes. Villa et al. (1996) found that there is an
616 extremely close correspondence between the Cl/Ca/K fingerprint deduced from the common-
617 denominator isotope correlation diagrams and the step ages (Fig. 7b-c). The second instance of an
618 artificial mineral mixture, discussed here, had been incompletely followed through by its proponents,
619 Kula et al. (2010). These authors reported the effect of artificially mixing two biotite samples, PM1 and

This is a preprint, the final version is subject to change, of the American Mineralogist (MSA)
Cite as Authors (Year) Title. American Mineralogist, in press.
(DOI will not work until issue is live.) DOI: http://dx.doi.org/10.2138/am-2017-6084

620 IV8, in variable mass ratios and concluded that no information could be gained on the mixing end-
621 members, as age spectra were discordant (Fig. 7d). On the contrary, the systematics established in
622 Figures 7b-c can be advantageously applied to the mixture of two heterochemical biotites by a more
623 goal-oriented plot of the original data (Kula et al. 2010, p. 74). While the age spectrum based only on
624 ^{39}Ar is discordant, the correlation between the ^{38}Ar/^{39}Ar (Cl/K) ratio and the age (Fig. 7e) reveals
625 almost ideal binary mixing (Villa 2001, his Fig. 2) and recovers the age of both end-members if the Ca,
626 Cl, and K concentrations are measured by EPMA. The reason why the age spectrum, based only on
627 ^{39}Ar, is insufficiently informative is that the differential release rates of the two biotite samples are
628 different (Fig. 7f). This distorts the mass balance of the summed Ar deriving in part from PM1 and in a
629 different proportion, variable from step to step, from IV8. The three-isotope correlation diagram in
630 Figure 7e does not suffer from this limitation and simply follows the algebraic rule valid for all binary
631 mixtures (Villa 2001).

632 Natural samples consisting of clear-cut polymineralic mixtures (approach B) display discordant
633 age spectra (Onstott et al. 1990; Villa et al. 2000). The variation range of the age spectrum of the
634 sample studied by Onstott et al. (1990) shows less extreme variations compared to the ^{39}Ar-^{40}Ar age
635 map obtained by laser ablation. Most importantly, the Cl/Ca/K fingerprint deduced from the common-
636 denominator isotope correlation diagrams follows the same pattern as the artificial mixtures of
637 approach (A). A natural sample that mimics the Wijbrans and McDougall (1986) mixture, when all five
638 Ar isotopes are analyzed, confirms and expands the findings of these authors and provides a
639 quantitative road map to deconvolve the muscovite and phengite end-members responsible for
640 discordant hump-shaped age spectra (Villa et al. 2014, their Fig. 9). A conception frequently heard is
641 that staircase-shaped age spectra reflect Ar loss, whereby it is often assumed (Hart 1964) that Ar loss is
642 always due to thermally activated diffusion. An example of a staircase-shaped age spectrum that
643 illuminates this issue is detrital white mica Rui9978 (Fig. 8a) that was burial-heated to $T < 300$ °C in
644 the sedimentary Houiller Basin in the French Western Alps (Villa et al. 2014, their Fig. 10 a-b). The

common denominator three-isotope correlation diagram (Fig. 8b) demonstrates that sample Rui9978 consists of two populations. EPMA identifies these populations to be intergrown on the μm scale. These consist of a detrital one, with high Si concentrations, and a metamorphic one, with high Al concentrations. The combination of EPMA analyses with the correlation diagrams establishes that recrystallization in a chemically open system involving mass transfer of cations, such as Al and Si, is the predominant cause of the low-temperature Ar loss in Rui9978.

The presence of natural mixtures among micas of different generations in metamorphic rocks opens a side-track on the optimum analytical approach to estimate the age of each generation. The first action required is obtaining microstructural/microchemical imaging and establishing the size, distribution and composition of the hetrogeneities. Recent observations (Berger et al. 2017) stress that in sheared rocks the retrogression/recrystallization products have a grain size < 10 μm (Fig. 9a-b), whereby the successive mica generations are tightly intergrown. Perhaps more surprisingly, "static" retrogression of an eclogite in the greenschist-facies also occurs very heterogeneously, on a scale < 10 μm (Fig. 9c). Given the impossibility to perform a mineral separation on a sieve fraction of < 10 μm, the next action required is choosing an analytical approach that maximizes the accuracy of the obtained information. As already pointed out by Müller et al. (2002, p. 73), ^{39}Ar-^{40}Ar analyses by laser ablation require a minumum sample size. Two contrasting requirements must be met. The beam size should be the smallest possible, in order to discriminate microstructures within a mineral and the sample size should be as large as possible, so that the counting statistics and the non-zero detection limit for ^{36}Ar have a small relative effect on the overall sum of the propagated uncertainties. The choice by Flude et al. (2014) of ablating areas ≥ (100 μm)^2 of a 470 Ma old K-feldspar is a compromise that gave an acceptable uncertainty of 0.5 %. In order to achieve similar precision on Cenozoic samples, larger beam sizes are necessary (Müller et al. 2002). The best spatial resolution of a laser-ablation ^{39}Ar-^{40}Ar analysis is not dictated by the laser beam diameter itself, but rather by the minimum sample size requirement, and is at least an order of magnitude larger than the typical size of the microstructures to

This is a preprint, the final version is subject to change, of the American Mineralogist (MSA)
Cite as Authors (Year) Title. American Mineralogist, in press.
(DOI will not work until issue is live.) DOI: http://dx.doi.org/10.2138/am-2017-6084

be dated (Figs. 9b,c). Therefore the volume of mineral ablated in a laser microprobe ^{39}Ar-^{40}Ar analysis will as a rule give a mixed age, as it contains all of the mineral generations of that sample. A way to disentangle heterochemical mineral generations is by associating stepwise heating of "large" samples (ca. 1-10 mg) to the Ca/Cl/K systematics provided by common-denominator three-isotope correlation diagrams (Fig. 7). Using this technique, Federico et al. (2005) were able to date both mica generations of the sample shown here in Figure 9c.

Case (C) has been observed only once in a natural sample, namely the gem-quality K-feldspar from Itrongay, Madagascar (Flude et al. 2014). The mineral is low sanidine (as defined following the structure refinement by Nyfeler et al. 1998), but can also be considered as orthoclase (e.g., Wartho et al. 1999). No stepwise heating spectrum was reported for the crystal rim piece for which the Ar* concentration profile was obtained. Stepheating was performed (Nyfeler et al. 1998; Villa, unpublished data, 1998) on one aliquot of the Itrongay K-feldspar crystal used by Wartho et al. (1999) to quantify the diffusive gradients caused by isothermal laboratory heating. One $(100\ \mu m)^3$ chip was heated in a resistance oven at 900 °C for 15 h. This chip was used by Nyfeler et al. (1998) to compare the respective rates of structural disordering and Ar loss. The chip then was irradiated, and subsequently degassed completely in 13 heating steps between 590 and 1530 °C. The total-gas K-Ar age of 94 Ma corresponds to a bulk Ar loss of 79 %. This bulk Ar loss prompted Nyfeler et al. (1998) to state that Ar loss is slower or equal to the Al,Si disordering rate. Since the experiments by Wartho et al. (1999) and Flude et al. (2014) demonstrate that the Itrongay gem-quality K-feldspar follows Fick's Law, whereby the diffusion length scale coincides with the physical grain size, it follows that in vacuo heating to 900 °C of the unirradiated K-feldspar chip that later was irradiated for the present experiment must have resulted in a bell-shaped diffusion profile. The laboratory degassing of Ar, whose spatial distribution follows a bell-shaped concentration gradient, can be modelled under the assumption that the degassing rate follows Fick's Law diffusion. The predicted age spectrum is shown in Figure 10 as a dashed line climbing to ca. 300 Ma.

695 The measured age spectrum, presented here as solid line in Figure 10, shows a subdued
696 staircase. The sub-optimum agreement between the diffusive degassing of the Ar spatial gradient and
697 the shape of the age spectrum is evidence that stepheating does not ensure a satisfactory recovery of the
698 spatial gradients that can only be quantified with laser-ablation ^{39}Ar-^{40}Ar analysis on a length scale of
699 several mm.

700 The physical mechanism of laboratory degassing is thus directly observed to be different from
701 that causing Ar loss in nature. Most natural samples that underwent rejuvenation are not recording
702 Fickian diffusion anyway (see above), but the question is, do laboratory stepheating experiments? The
703 answer is provided by the context of the Itrongay K-feldspar experiments. The Itrongay pegmatite
704 hosting the K-feldspar did undergo a prolonged medium-temperature history (500-600 °C?), which was
705 so dry that the K-feldspar was not retrogressed to deuterically coarsened perthite (an exceptional
706 instance: Plümper and Putnis 2009), and gave rise to the only bell-shaped ^{40}Ar diffusion profile
707 observed so far (Flude et al. 2014). Degassing by stepheating between 590 °C and 1530 °C did not
708 recover the bell-shaped profile, hence had not followed Fickian diffusion. An explanation originally
709 proposed by Hetherington and Villa (2007) assigns a pivotal role to structural rearrangement of the
710 silica tetrahedra, phonons, and one or more unquenchable phase transitions (Laves 1956). The
711 existence of phonons and phase transitions was unknown to Fick when he formulated his Law
712 quantifying nutrient transport in aqueous solutions in the mid 19th century.

713 The available petrological data show that the discordance of ^{39}Ar-^{40}Ar age spectra is always
714 dominated by heterochemical phase mixtures, which can only be correctly diagnosed by using isotope
715 correlation plots that take into account both textural images obtained by various techniques (CL, BSE,
716 EPMA X-ray maps) and measuring all five Ar isotopes. In the only instance reported so far of a truly
717 monomineralic sample, in which a bell-shaped age gradient was documented by laser-ablation ^{39}Ar-
718 ^{40}Ar analysis, the stepheating protocol does not yield a staircase-shaped age spectrum reminiscent of
719 the known intra-grain ^{40}Ar* distribution.

This is a preprint, the final version is subject to change, of the American Mineralogist (MSA)
Cite as Authors (Year) Title. American Mineralogist, in press.
(DOI will not work until issue is live.) DOI: http://dx.doi.org/10.2138/am-2017-6084

720

721 **Implications**

722

723 A change of paradigm in geochronology has been slowly emerging in recent years. As more
724 detailed high-resolution petrologic imaging and mapping has shown the complexity of natural
725 materials, early physical models of isotope transport based on simplifying assumptions have been
726 superseded by more articulate views based on the labor-intensive establishment of a context between
727 mineral petrogenesis, microstructural constraints, and intra-grain chemical and isotopic disequilibria. It
728 is still true that the U-Pb, Rb-Sr, and K-Ar isotopic systems share deep-reaching similarities, as already
729 was thought half a century ago by Wetherill (1963) and Hart (1964). However, in complete antithesis to
730 the hypotheses formulated at that time, the similarities do not lie in the fact that in these systems age
731 discordance is caused by Fick's Law diffusion at high temperature, but in the fact that in both U-Pb and
732 K-Ar age discordance is principally due to mixing heterochemical, diachronous phases. Since volume
733 diffusion is orders of magnitude slower than dissolution/reprecipitation at most metamorphic
734 temperatures, it plays a subordinate role whenever circulating fluids are available to promote
735 retrogressive reactions.

736 The mineralogy of the mineral geochronometers reflects first and foremost the petrologic
737 conditions. To the extent that patchy chemical and crystallographic zonations are observed, it is self-
738 evident that diffusive re-equilibration was at most incomplete, if not negligible, whereas fluid-assisted
739 recrystallization was predominant. Therefore, the main control on the isotopic record of mineral
740 geochronometers is the latter, not the former. Microstructural observations associated with chemical
741 microanalyses ubiquitously document that, as a rule, patchy retrogression textures are associated with
742 heterochemical signatures (U/Th ratios, REE patterns, Ca/Cl/K ratios) and thus provide firm evidence
743 of a chemically open system during the reactions that caused petrologic disequilibrium. The geological

744 interpretation of age discordance requires an intensive mineralogical-petrological framework, as
745 discordance is caused by mixtures of heterochemical, resolvably diachronous, mineral generations.
746
747 **Acknowledgements**
748
749 Detailed reviews by D.E. Harlov, A.R. Heri and two anonymous reviewers helped clarify many
750 descriptions of actual observations. A. Berger provided the two images of sample Ga142 presented in
751 Figure 9. Thanks to G. Dunning for many fruitful discussion on U-Pb geochronology, and to M. J.
752 Whitehouse for doing the SIMS analyses presented in Figure 3.
753
754 **References**
755
756 Arnaud, N.O., and Eide, E.A. (2000) Brecciation-related argon redistribution in alkali feldspars: An in naturo crushing study. Geochimica
757 et Cosmochimica Acta, 64, 3201-3215.
758 Berger, A., Wehrens, P., Lanari, P., Zwingmann, H., and Herwegh, M. (2017) Microstructures, mineral chemistry and geochronology of
759 white micas along a retrograde evolution: An example from the Aar massif (Central Alps, Switzerland). Tectonophysics, in
760 press.
761 Bingen, B., and van Breemen, O. (1998) U-Pb monazite ages in amphibolite- to granulite-facies orthogneiss reflect hydrous mineral
762 breakdown reactions: Sveconorwegian Province of SW Norway. Contributions to Mineralogy and Petrology, 132, 336-353.
763 Bracciali, L., Parrish, R.R., Horstwood, M.S.A., Condon, D.J., Najman, Y. (2013) U–Pb LA-(MC)-ICP-MS dating of rutile: new
764 reference materials and applications to sedimentary provenance. Chemical Geology, 347, 82–101.
765 Chafe, A.N., Villa I.M., Hanchar J.M., Wirth R. (2014) A re-examination of petrogenesis and $^{40}Ar/^{39}Ar$ systematics in the the Chain of
766 Ponds K-feldspar: "diffusion domain" archetype versus polyphase hygrochronology. Contributions to Mineralogy and Petrology
767 167(5), 1010.
768 Cherniak, D.J. (1993) Lead diffusion in titanite and preliminary results on the effects of radiation damage on Pb transport. Chemical
769 Geology, 110, 177-194.
770 Cherniak, D.J. (2000) Pb diffusion in rutile. Contributions to Mineralogy and Petrology, 139, 198–207.
771 Cherniak, D.J. (2010) Diffusion in accessory minerals: zircon, titanite, apatite, monazite and xenotime. In Y. Zhang and D.J. Cherniak,
772 Eds., Diffusion in minerals and melts. Reviews in Mineralogy & Geochemistry, 72, 827-869.

773 Cherniak, D.J., Lanford ,W.A., and Ryerson, F.J. (1991) Lead diffusion in apatite and zircon using ion implantation and Rutherford
774 backscattering techniques. Geochimica et Cosmochimica Acta 55, 1663-1673.
775 Cherniak, D.J., and Watson, E.B. (2000) Pb diffusion in zircon. Chemical Geology, 172, 5–24.
776 Chew, D.M. Petrus, J A., Kenny, G.G., and McEvoy, N. (2017) Rapid high-resolution U–Pb LA-Q-ICPMS age mapping of zircon.
777 Journal of Analytical Atomic Spectrometry, 32, 262-276.
778 Cocherie, A., Legendre, O., Peucat, J.J., and Kouamelan, A.N. (1998) Geochronology of polygenetic monazites constrained by in situ
779 electron microprobe Th-U-total lead determination: Implications for lead behaviour in monazite. Geochimica et Cosmochimica
780 Acta, 62, 2475-2497.
781 Condon, D.J., Schoene, B., McLean, N.M., Bowring, S.A., and Parrish, R.R. (2016) Metrology and traceability of U-Pb isotope dilution
782 geochronology (EARTHTIME Tracer Calibration Part I). Geochimica et Cosmochimica Acta, 164, 464-480.
783 Corfu, F. (2013) A century of U-Pb geochronology: The long quest towards concordance. Geological Society of America Bulletin, 125,
784 33-47, doi: 10.1130/B30698.1
785 Corfu, F., and Stone, D. (1998) The significance of titanite and apatite U-Pb ages: Constraints for the post-magmatic thermal-
786 hydrothermal evolution of a batholithic complex, Berens River area, northwestern Superior Province, Canada. Geochimica et
787 Cosmochimica Acta, 92, 2979–2995.
788 Corfu, F., Hanchar, J.M., Hoskin, P.W.O., and Kinny, P. (2003) Atlas of zircon textures. In J.M. Hanchar and P.W.O. Hoskin, Eds.,
789 Zircon. Reviews in Mineralogy & Geochemistry, 53, 469-500.
790 Crank, J. (1975) The mathematics of diffusion. Clarendon Press, Oxford, 414 p.
791 DeWolf, C.P., Belshaw, N., and O'Nions, R.K. (1993) A metamorphic history from micron-scale $^{207}Pb/^{206}Pb$ chronometry of Archean
792 monazite. Earth and Planetary Science Letters, 120, 207-220.
793 Dohmen, R., Chakraborty, S., Palme, H., and Rammensee, W. (1998) Solid-solid reactions mediated by a gas phase: An experimental
794 study of reaction progress and the role of surfaces in the system olivine+iron metal. American Mineralogist, 83, 970-984.\
795 Ellsworth, S., Navrotsky, A., and Ewing, R.C. (1994) Energetics of radiation damage in natural zircon ($ZrSiO_4$). Physics and Chemistry
796 of Minerals, 21, 140-149.
797 Faure, G. (1986) Principles of Isotope Geology, 2nd ed., 464 p. Wiley, Chichester.
798 Federico, L., Capponi, G., Crispini, L., Scambelluri, M., and Villa, I.M. (2005) $^{39}Ar/^{40}Ar$ dating of high-pressure rocks from the Ligurian
799 Alps: evidence for a continuous subduction-exhumation cycle. Earth and Planetary Science Letters, 240, 668-680.
800 Fisher, C.M., Hanchar, J.M., Miller, C.F., Phillips, S.E., Vervoort, J., and Whitehouse, M.J. (2017) Combining Nd isotopes in monazite
801 and Hf isotopes in zircon to understand complex open-system processes in granitic magmas. Geology, 45: doi:
802 10.1130/G38458.1.
803 Fitch, F.J., Miller, J.A., and Mitchell, J.G. (1969) A new approach to radio-isotopic dating in orogenic belts. Geological Society of
804 London Special Publications, 3, 157-195.

805 Flude, S., Halton, A.M., Kelley, S.P., Sherlock S.C., Schwanethal, J., and Wilkinson, C.M. (2014) Observation of centimetre-scale argon
806 diffusion in alkali feldspars: implications for $^{40}Ar/^{39}Ar$ thermochronology. Geological Society of London Special Publications,
807 378, 265-275.
808 Gebauer, D., Quadt, A.v., Compston, W., Williams, I.S., and Grünenfelder, M. (1988) Archean zircons in a retrograded Caledonian
809 eclogite of the Gotthard massif (Central Alps, Switzerland). Schweizerische Mineralogische und Petrographische Mitteilungen,
810 68, 485-490.
811 Giletti, B.J. (1974) Studies in diffusion I: argon in phlogopite mica. In A.W. Hofmann, B.J. Giletti, H.S. Yoder and R.A. Yund, Eds.,
812 Geochemical Transport and Kinetics. Carnegie Institution of Washington Publication, 634, 107-115.
813 Giletti, B.J., and Tullis, J. (1977) Studies in diffusion, IV. Pressure dependence of Ar diffusion in phlogopite mica. Earth and Planetary
814 Science Letters, 35, 180-183.
815 Glodny, J., Kuhn, A., and Austrheim, H. (2008) Diffusion versus recrystallization processes in Rb-Sr geochronology: isotopic relics in
816 eclogite facies rocks, Western Gneiss region, Norway. Geochimica et Cosmochimica Acta, 72, 506-525.
817 Goudie, D.J., Fisher, C.M., Hanchar, J.M., Crowley, J.L., and Ayers, J.C. (2014) Simultaneous in situ determination of U-Pb and Sm-Nd
818 isotopes in monazite by laser ablation ICP-MS. Geochemistry, Geophysics, Geosystems, 15, 2575-2600.
819 Gregory, C.J., McFarlane, C.R.M., Hermann, J., and Rubatto, D., 2009, Tracing the evolution of calc-alkaline magmas: In-situ Sm-Nd
820 isotope studies of accessory minerals in the Bergell Igneous Complex, Italy. Chemical Geology, 260, 73–86.
821 Grove, M., and Harrison, T. (1999) Monazite Th–Pb age depth profiling. Geology, 27, 487-490.
822 Gruber, C., Kutuzov, I., and Ganor, J. (2016) The combined effect of temperature and pH on albite dissolution rate under far-from-
823 equilibrium conditions. Geochimica et Cosmochimica Acta, 186, 154-167.
824 Hanchar, J.M., and Miller, C.F. (1993) Zircon zonation patterns as revealed by cathodoluminescence and back-scattered electron images:
825 implications for interpretation of complex crustal histories. Chemical Geology, 110, 1-13.
826 Hanchar, J.M., and Rudnick, R.L. (1995) Revealing hidden structures: the application of cathodoluminescence and back-scattered
827 electron imaging to dating zircons from lower crustal xenoliths. Lithos, 36, 289-303.
828 Harlov, D.E., and Hetherington, C.J. (2010) Partial high-grade alteration of monazite using alkali-bearing fluids: Experiment and nature.
829 American Mineralogist, 95, 1105-1108.
830 Harlov, D.E., Wirth, R., and Hetherington, C.J. (2007) The relative stability of monazite and huttonite at 300–900°C and 200–1000 MPa:
831 Metasomatism and the propagation of metastable mineral phases. American Mineralogist, 92, 1652–1664.
832 Harlov, D. E., Wirth, R., and Hetherington, C.J. (2011), Fluid-mediated partial alteration in monazite: The role of coupled dissolution-
833 reprecipitation in element redistribution and mass transfer. Contributions to Mineralogy and Petrology, 162, 329–348.
834 Hart S.R. (1964) The petrology and isotopic-mineral age relations of a contact zone in the Front Range, Colorado. Journal of Geology, 72,
835 493–525.
836 Hawkins, D.P., and Bowring, S.A. (1997) U-Pb systematics of monazite and xenotime: case studies from the Paleoproterozoic of the
837 Grand Canyon, Arizona. Contributions to Mineralogy and Petrology, 127, 87-103.

838 Hetherington, C.J., and Harlov, D.E. (2008) Partial metasomatic alteration of xenotime and monazite from a granitic pegmatite, Hidra
839 anorthosite massif, southwestern Norway: Dissolution-reprecipitation and the subsequent formation of thorite and uraninite
840 inclusions. American Mineralogist, 93, 806–820.
841 Hetherington, C.J., and Villa, I.M. (2007) Barium silicates of the Berisal Complex, Switzerland: A study in geochronology and rare-gas
842 release systematics. Geochimica et Cosmochimica Acta, 71, 3336-3347.
843 Hodges, K.V., Hames, W.E., and Bowring, S.A. (1994) $^{40}Ar/^{39}Ar$ age gradients in micas from a high-temperature-low-pressure
844 metamorphic terrain; evidence for very slow cooling and implications for the interpretation of age spectra. Geology, 22, 55-58.
845 Huyskens, M.H., Zink, S., and Amelin, Y. (2016) Evaluation of temperature-time conditions for the chemical abrasion treatment of single
846 zircons for U–Pb geochronology. Chemical Geology, 428, 25-35.
847 Jäger, E. (1967) Die Bedeutung der Biotit Alterswerte. In: Jäger, E., Niggli, E. & Wenk, E. (eds.). Altersbestimmungen an Glimmern in
848 den Zentralalpen. Beiträge zur Geologischen Karte, Neue Folge, 134, 11-21.
849 Jamtveit, B. (2010) Metamorphism: from patterns to processes. Elements, 6, 149-152.
850 Jeffery, P. M., and Reynolds, J.H. (1961) Origin of excess Xe129 in stone meteorites. Journal of Geophysical Research, 66, 3582–3583.
851 Kooijman, E., Mezger, K., and Berndt, J. (2010) Constraints on the U–Pb systematics of metamorphic rutile from in situ LA-ICP-MS
852 analysis. Earth and Planetary Science Letters, 293, 321–330.
853 Krogh, T.E. (1970) A simplified technique for the dissolution of zircon and the isolation of uranium and lead. Carnegie Institution of
854 Washington Yearbook, 69, 342-344.
855 Krogh, T.E. (1971) A low contamination method for decomposition of zircon and the extraction of U and Pb for isotopic age
856 determinations. Carnegie Institution of Washington Yearbook, 70, 258-288.
857 Krogh, T.E (1973) A low-contamination method for hydrothermal decomposition of zircon and extraction of U and Pb for isotopic age
858 determinations. Geochimica et Cosmochimica Acta, 37, 485-494.
859 Krogh, T.E (1982a) Improved accuracy of U-Pb zircon dating by selection of more concordant fractions using a high gradient magnetic
860 separation technique, Geochimica et Cosmochimica Acta, 46, 631-635.
861 Krogh, T.E (1982b) Improved accuracy of U-Pb zircon ages by the creation of more concordant systems using an air abrasion technique,
862 Geochimica et Cosmochimica Acta, 46, 637-649.
863 Krogh, T.E., and Davis, D. (1975). Alteration in zircons and differential dissolution of altered and metamict zircon. Carnegie Institution
864 of Washington Yearbook, 74, 619-623.
865 Kula, J., Spell, T.L., and Zanetti, K.A. (2010) $^{40}Ar/^{39}Ar$ analyses of artificially mixed micas and the treatment of complex age spectra
866 from samples with multiple mica populations. Chemical Geology, 275, 67-77.
867 Kusiak, M.A., Whitehouse, M., Wilde, S.A., Nemchin, A.A., and Clark, C. (2013) Mobilization of radiogenic Pb in zircon revealed by
868 ion imaging: Implications for early Earth geochronology. Geology, 41, 291-294.
869 Labotka, T.C., Cole, D.R., Fayek, M., Riciputi, L.R., and Stadermann, F.J. (2004) Coupled cation and oxygen-isotope exchange between
870 alkali feldspar and aqueous chloride solution. American Mineralogist, 89, 1822-1825.

Laurent A.T., Seydoux-Guillaume A.M., Duchêne S., Bingen B., Bosse V., Datas L. (2016) Sulphate incorporation in monazite lattice and dating the cycle of sulphur in metamorphic belts. Contributions to Mineralogy and Petrology, 171, 94.

Laves, F. (1956) Über die Bedeutung der Barbierit-Analbit-Umwandlung (displacive transformation) für die Erscheinungsformen der Feldspäte in Larvikiten und Rhombenporphyren. Zeitschrift für Kristallographie, 107, 196-201.

McLaren, A.C., FitzGerald, J.C., Williams, I.S. (1994) The microstructure of zircon and its influence on the age determination from Pb/U isotopic ratios measured by ion microprobe. Geochimica et Cosmochimica Acta, 58, 993–1005.

Mattinson, J.M. (2005) Zircon U–Pb chemical abrasion (‘‘CA–TIMS’’) method: combined annealing and multi-step dissolution analysis for improved precision and accuracy of zircon ages. Chemical Geology, 220, 47–66.

Mattinson, J.M. (2011) Extending the Krogh legacy: development of the CA–TIMS method for zircon U–Pb geochronology. Canadian Journal of Earth Sciences, 48, 95–105.

McFarlane, C.R.M., and McCulloch, M.T. (2007) Coupling of in-situ Sm-Nd systematics and U-Pb dating of monazite and allanite with application to crustal evolution studies, Chemical Geology, 245, 45–60.

McLean, N.M., Condon, D.J., Schoene, B., and Bowring, S.A. (2016) Evaluating uncertainties in the calibration of isotopic reference materials and multi-element isotopic tracers (EARTHTIME Tracer Calibration Part II). Geochimica et Cosmochimica Acta, 164, 481-501.

Merrihue, C.M. (1965) Trace-element determinations and potassium-argon dating by mass spectroscopy of neutron-irradiated samples. Transactions of the American Geophysical Union, 46, 125.

Merrihue, C.M., and Turner, G. (1966) Potassium-argon dating by activation with fast neutrons. Journal of Geophysical Research, 71, 2852-2857.

Mezger, K., and Krogstadt, E.J. (1997) Interpretation of discordant zircon ages: an evaluation. Journal of Metamorphic Geologym 15, 127-140.

Miller, J.S., Matzel, J.E.P., Miller, C.F., Burgess, S.D., and Miller, R.B. (2007) Zircon growth and recycling during the assembly of large, composite arc plutons. Journal of Volcanology and Geothermal Research, 167, 282-299.

Mitchell J.G. (1968) The argon-40/argon-39 method for potassium-argon age-determination. Geochimica et Cosmochimica Acta, 32, 781-790.

Möller, A., O'Brien, P.J., Kennedy, A., and Kröner, A. (2002) Polyphase zircon in ultrahigh-temperature granulites (Rogaland, SW Norway): constraints for Pb diffusion in zircon. Journal of Metamorphic Geology, 20, 727–740.

Müller, W., Kelley S.P., Villa I.M., 2002. Dating fault-generated pseudotachylytes: Comparison of 40Ar/39Ar stepwise-heating, laser-ablation and Rb/Sr microsampling analyses. Contributions to Mineralogy and Petrology, 144, 57-77.

Mundil, R., Ludwig, K.R., Metcalfe, I., and Renne, P.R. (2004) Age and timing of the Permian mass extinctions: U/Pb dating of closed-system zircons. Science, 305, 1760-1763.

Nasdala, L., Hanchar, J.M., Rhede D., Kennedy, A.K. and Váczi, T. (2010) Complex alteration of zircon: An example from Bancroft, Ontario. Chemical Geology, 269, 290-300.

Nemchin, A.A., Horstwood, M.S.A., and Whitehouse, M.J. (2013) High-spatial-resolution geochronology. Elements, 9, 31-37.

Nyfeler, D., Armbruster, T., and Villa, I.M. (1998) Si, Al, Fe order-disorder in Fe-bearing K-feldspar from Madagascar and its implication to Ar diffusion. Schweizerische Mineralogische und Petrographische Mitteilungen, 78, 11-21.

Onstott, T.C., Phillips, D., and Pringle-Goodell, L. (1991) Laser microprobe measurement of chlorine and argon zonation in biotite. Chemical Geology, 90, 145-168.

Parrish, R.R. (1990) U-Pb dating of monazite and its application to geological problems. Canadian Journal of Earth Sciences, 27, 1431–1450.

Paquette, J.L., and Tiepolo, M. (2007) High resolution (5 μm) U–Th–Pb isotope dating of monazite with excimer laser ablation (ELA)-ICPMS. Chemical Geology, 240, 222–237.

Paterson, B.E., Stephens, W.E., and Herd, D.A. (1989) Zoning in granitoid accessory minerals as revealed by backscattered electron imagery. Mineralogical Magazine, 53, 55- 62.

Paterson, B.A., Rogers, G., and Stephens, W.E. (1992a) Evidence for inherited Sm-Nd isotopes in granitoid zircons. Contributions to Mineralogy and Petrology, 111, 378-390.

Paterson, B.A., Stephens, W.E., Rogers, G., Williams, I.S., Hinton, R.W., and Herd, D.A. (1992b) The nature of zircon inheritance in two granite plutons. Transactions of the Royal Society of Edinburgh, Earth Sciences, 83, 459-471.

Paul, B., Woodhead, J.D., Paton, C., Hergt, J.M., Hellstrom J., and Norris, C.A. (2012) Multi-phase assemblages: Mineral identification and analysis correction procedures. Geostandards and Geoanalytical Research, 38, 253-263.

Petrus, J.A., Chew, D.M., Leybourne, M.I. Kamber, B.S. (2017) A new approach to laser-ablation inductively-coupled-plasma mass-spectrometry (LA-ICP-MS) using the flexible map interrogation tool 'Monocle'. Chemical Geology, 463, 76-93.

Phillips, D., and Onstott, T.C. (1988) Argon isotopic zoning in mantle phlogopite. Geology, 16, 542-546.

Piazolo, S., Austrheim, H., and Whitehouse, M.J. (2012) Brittle-ductile microfabrics in naturally deformed zircon: Deformation mechanisms and consequences for U-Pb dating. American Mineralogist, 97, 1544–1563.

Piazolo, S., La Fontaine, A., Trimby, P., Harley, S., Yang, L., Armstrong, R., and Cairney, J.M. (2016) Deformation-induced trace element redistribution in zircon revealed using atom probe tomography. Nature Communications, 7, 10490.

Plümper, O., and Putnis, A. (2009) The Complex Hydrothermal History of Granitic Rocks: Multiple Feldspar Replacement Reactions under Subsolidus Conditions. Journal of Petrology, 50, 967-987.

Putnis, A. (2002) Mineral replacement reactions: from macroscopic observations to microscopic mechanisms. Mineralogical Magazine, 66, 689-708.

Putnis, A. (2009) Mineral replacement reactions. In E.H. Oelkers and J. Schott, Eds., Thermodynamics and Kinetics of Water-Rock Interaction. Reviews in Mineralogy & Geochemistry, 70, 87-124.

Putnis, A., and Austrheim, H. (2013) Mechanisms of metasomatism and metamorphism on the local mineral scale: The role of Dissolution-Reprecipitation during mineral re-equilibration. In D.E. Harlov and H. Austrheim, Eds., Metasomatism and the Chemical Transformation of Rock, p. 141-170. Springer, Heidelberg.

Reynolds, J.H. (1963) Xenology. Journal of Geophysical Research, 68, 2939-2956.

Rittner, M., and Müller, W. (2012) 2D mapping of LA-ICPMS trace element distributions using R. Computers and Geosciences, 42, 152-161.

Romer, R.L. (1996) U-Pb systematies of stilbite-bearing low-temperature mineral assemblages from the Malmberget iron ore, northern Sweden. Geochimica et Cosmochimica Acta, 60, 1951-1961.

Schoene, B., Latkoczy, C., Schaltegger, U., and Günter, D. (2010) A new method integrating high-precision U-Pb geochronology with zircon trace element analysis (U-Pb TIMS-TEA). Geochimica et Cosmochimica Acta, 74, 7144-7159.

Silver, L.T., and Deutsch, S. (1963) Uranium-lead isotopic variations in zircon: a case study. Journal of Geology, 71, 721-758.

Steiger, R.H., Bickel, R.A., and Meier, M. (1993) Conventional U-Pb dating of single fragments of zircon for petrogenetic studies of Phanerozoic granitoids. Earth and Planetary Science Letters, 115, 197-209.

Stern, R.A., and Berman, R.G. (2001) Monazite U–Pb and Th–Pb geochronology by ion microprobe, with an application to in situ dating of an Archean metasedimentary rock. Chemical Geology, 172, 113-130.

Tartèse, R., Ruffet, G., Poujol, M., Boulvais, P., and Ireland, T.R. (2011) Simultaneous resetting of the muscovite K-Ar and monazite U-Pb geochronometers: a story of fluids. Terra Nova, 23, 390-398.

Tera, F., and Wasserburg, G.J. (1972a) U-Th-Pb systematics in three Apollo 14 basalts and the problem of initial Pb in lunar rocks: Earth and Planetary Science Letters, 14, 281–304.

Tera, F. and Wasserburg G.J. (1972b) U–Th–Pb systematics in lunar highland samples from the Luna 20 and Apollo 16 missions. Earth and Planetary Science Letters 17, 36–51.

Tilton, G.R. (1960) Volume diffusion as a mechanism for discordant lead ages. Journal of Geophysical Research, 65, 2933-2945.

Turner, G. (1965) Extinct Iodine 129 and trace elements in chondrites. Journal of Geophysical Research, 70, 5433-5445.

Turner, G., Huneke, J.C., Podosek, F.A., and Wasserburg, G.J. (1971) ^{40}Ar-^{39}Ar ages and cosmic ray exposure age of Apollo 14 samples. Earth and Planetary Science Letters, 12, 19-35.

Ubide, T., McKenna, C.A., Chew, D.M., and Kamber, B.S. (2015) High-resolution LA-ICP-MS trace element mapping of igneous minerals. Chemical Geology, 409, 157-168.

Valley, J.W., Cavosie, A.J., Ushikubo, T., Reinhard, D.A., Lawrence, D.F., Larson, D.J., Clifton, P.H., Kelly, T.F., Wilde, S.A., Moser, D.E., and Spicuzza, M.J. (2014) Hadean age for a post-magma-ocean zircon confirmed by atom-probe tomography. Nature Geoscience, 7, 219-223.

Vavra, G. (1990) On the kinematics of zircon growth and its petrogenetic significance: a cathodoluminescence study. Contributions to Mineralogy and Petrology, 106, 90-99.

Vavra, G., and Hansen, B.T. (1991) Cathodoluminescence studies and U/Pb dating of zircons in pre-Mesozoic gneisses of the Tauern Window: Implications for the Penninic basement evolution. Geologische Rundschau, 80, 703-715.

Villa, I.M. (2001) Radiogenic isotopes in fluid inclusions. Lithos, 55, 115-124.

Villa, I.M. (2006) From the nm to the Mm: isotopes, atomic-scale processes, and continent-scale tectonic models. Lithos, 87, 155-173.

970 Villa, I.M. (2010) Disequilibrium Textures vs Equilibrium Modelling: Geochronology at the Crossroads. In M.I. Spalla, A.M. Marotta
971 and G. Gosso, Eds., Advances in Interpretation of Geological Processes. Geological Society of London Special Publications, 332,
972 1-15.
973 Villa, I.M. (2016) Diffusion in mineral geochronometers: present and absent. Chemical Geology, 420, 1-10.
974 Villa, I.M., and Puxeddu, M. (1994) Geochronology of the Larderello geothermal field: new data and the "closure temperature" issue.
975 Contributions to Mineralogy and Petrology, 115, 415-426.
976 Villa, I.M., and Williams, M.L., 2013. Geochronology of metasomatic events. In D.E. Harlov and H. Austrheim, Eds., Metasomatism and
977 the Chemical Transformation of Rock, p. 171-202. Springer, Heidelberg.
978 Villa, I.M., Grobéty, B., Kelley, S.P., Trigila, R., and Wieler, R. (1996) Assessing Ar transport paths and mechanisms for McClure
979 Mountains Hornblende. Contributions to Mineralogy and Petrology, 126, 67-80.
980 Villa, I.M., Hermann, J., Müntener, O., and Trommsdorff, V. (2000) ^{39}Ar-^{40}Ar dating of multiply zoned amphibole generations (Malenco,
981 Italian Alps). Contributions to Mineralogy and Petrology, 140, 363-381.
982 Villa, I.M., Bucher, S., Bousquet, R., Kleinhanns, I.C., and Schmid, S.M. (2014) Dating polygenetic metamorphic assemblages along a
983 transect through the Western Alps. Journal of Petrology, 55, 803-830.
984 Wartho, J.A., Kelley, S.P., Brooker, R.A., Carroll, M.R., Villa, I.M., and Lee, M.R. (1999) Direct Ar diffusion measurements in a gem-
985 quality Madagascar K-feldspar using the Ultra-Violet Laser Ablation Microprobe (UVLAMP). Earth and Planetary Science
986 Letters, 170, 141-153.
987 Wetherill, G.W. (1956) Discordant Uranium-Lead Ages 1. Transactions, American Geophysical Union, 37, 320-326.
988 Wetherill, G.W. (1963) Discordant Uranium-Lead Ages 2. Discordant Ages Resulting from Diffusion of Lead and Uranium. Journal of
989 Geophysical Research, 68, 2957-2965.
990 Whitehouse, M.J., Kumar, G.R.R., and Rimša, A. (2014) Behaviour of radiogenic Pb in zircon during ultrahigh-temperature
991 metamorphism: an ion imaging and ion tomography case study from the Kerala Khondalite Belt, southern India. Contributions
992 to Mineralogy and Petrology, 168, 1-18.
993 Wijbrans, J.R., and McDougall, I. (1986) Ar-40/Ar-39 dating of white micas from an Alpine high-pressure metamorphic belt on Naxos
994 (Greece) - the resetting of the argon isotopic system. Contributions to Mineralogy and Petrology, 93, 187-194.
995 Williams, M.L., Jercinovic, M.J., and Hetherington, C.J. (2007) Microprobe monazite geochronology: Understanding geologic processes
996 by integrating composition and chronology. Annual Reviews in Earth and Planetary Science, 35, 137-175.
997 Williams, M.L., Jercinovic, M.J., Harlov, D.E., Budzyń, B., and Hetherington, C.J. (2011) Resetting monazite ages during fluid-related
998 alteration. Chemical Geology, 283, 218-225.
999 Wood, B.J., and Walther, J.V. (1983) Rates of hydrothermal reactions. Science, 222, 413-415.
1000 Zhou, L., McKenna, C.A., Long, D.G.F., Kamber, B.S. (2017) LA-ICP-MS elemental mapping of pyrite: An application to the
1001 Palaeoproterozoic atmosphere. Precambrian Research, 297, 22-55.

1002

1003 **Figure Captions**

1004

1005 Fig. 1 - Concordia diagram following Wetherill (1956). The solid black curve with the ages (given in
1006 Ma) marked with red dots is referred to as the concordia curve. It is the geometric locus of all points
1007 whose two U-Pb ages are concordant. The green ellipse represents the analysis of such a "concordant"
1008 sample, which crystallized 2000 Ma ago. The orange ellipse, which lies significantly off the concordia,
1009 represents the analysis of a sample whose ^{238}U-^{206}Pb age is lower than the ^{235}U-^{207}Pb age; the
1010 chronological information that can be extracted from this sample is not straightforward.

1011

1012 Fig. 2 - Rates of relevant processes affecting the U-Pb and K-Ar systems. Solid lines: Pb diffusivity in
1013 apatite (Cherniak et al. 1991) and corrected Ar diffusivity in phlogopite (Giletti 1974; Villa 2010).
1014 Within stated uncertainty, the slopes of the phlogopite and apatite lines are indistinguishable at the 1
1015 sigma level. Dashed line: dissolution rate of silicates in water (Wood and Walther 1983), which
1016 coincides with the Pb*, Sr, and Ar loss rate of reacting silicates, as incompatible daughter isotopes are
1017 lost upon dissolution. Dash-dotted line: Ar loss rate from the Hart (1964) original data corrected for
1018 variable grain size and cylindrical geometry. Both the *a priori* arguments for a chemically open aureole
1019 mentioned in the text and the parallelism of the Sr and Ar loss rate to the aqueous dissolution rate of the
1020 silicates are conclusive *a posteriori* evidence that Hart (1964) misinterpreted the isotopic evidence for
1021 Fick's Law of diffusion. Argon loss from the Eldora samples was dominated by the aqueous dissolution
1022 quantified by Wood and Walther (1983), as the Ar diffusivity in phlogopite, proposed by Giletti (1974),
1023 is several orders of magnitude slower. Pb diffusivity in apatite is marginally slower.

1024

1025 Fig. 3 - Wetherill (1956) Concordia diagram with back-scattered electron image of a zircon crystal
1026 from a Cretaceous peraluminous granite. Inset: crystal showing locations of SIMS analysis. The

analysis locations were selected intentionally to analyze the rim, core, and to straddle the rim-core boundary. This crystal illustrates that the core of a zircon crystal is often not in the geometric center of the grain, that it forms an angular unconformity with its overgrowths, and that the thickness of the rim varies significantly throughout the crystal.

Fig. 4 - Concordia diagrams showing different ways to plot U-Pb data. (a) Wetherill (1956) Concordia diagram. The schematic representation of Fig. 1 is augmented by a listing of possible causes of discordance. Two clusters of concordant data-points are shown, one at 2000 Ma (labelled "igneous or metamorphic cores") and one at 1000 Ma (labelled "igneous or metamorphic rims"), with reference to their growth sequence in individual grains. Discordant data-points are color coded with respect to the geological/mineralogical cause of discordance, as are the trajectories that displace data-points from concordia. High-temperature diffusive Pb* loss is not represented because it has not been observed in natural zircon and monazite samples. Instead, the dominant cause of discordance is the physical mixing of young rims and old cores (e.g., Mezger and Krogstadt 1997), shown by the dashed orange line and the orange ellipses. The caption "large/small" rims and cores refers to the mass balance of the U in core and rim, not to their volume: a thin rim with very high U concentration can host most of the grain's U and will accordingly drag the physical mixture far towards the lower left. The caption "low-T Pb* loss" points out that old, metamict cores can undergo a loss of Pb* by interacting with aqueous fluids in near-surface or low-grade conditions. This loss of Pb* can occur at the present day (blue dashed line, blue ellipses) or can have occurred at some time in the past (orange caption), concurrently with the formation of metamorphic rims. The grey dashed line represents a mineralogical/geochemical disturbance, whereby very small inclusions rich in non-radiogenic Pb are included in the U-rich, Pb-poor chronometer grains. The two-arrowed red line represents an analytical artefact that can be observed in microbeam analyses (more frequently in laser ablation plasma source mass spectrometry, sometimes also in secondary ion mass spectrometry): U and Pb are vaporized from the matrix and

ionized at different rates from each other and from those in the reference material used for calibration, achieving either an artificial U loss+Pb gain, or an artificial Pb loss+U gain. Finally, the two purple ellipses labelled "ambiguous" are data-points that are analytically indistinguishable from the concordia, but give a different age than the cluster of green ellipses. Interpreting their age (e.g., in terms of protracted magmatogenesis) requires establishing a context with non-chronometric indicators, such as trace element patterns (e.g. Schoene et al. 2010). - (b) Tera-Wasserburg Concordia diagram (Tera and Wasserburg, 1972a,b). The curve with the ages marked with red dots is also a concordia curve, as it is the locus of concordant data-points. This alternative diagram is similar in principle to Fig. 4a but is based on the $^{207}Pb/^{206}Pb$ vs. $^{238}U/^{206}Pb$ relation. The color-coding of the relevant causes and trajectories of discordance is the same as in Fig. 4a.

Fig. 5 - (**a**) Age spectra of two subsamples of lunar rock 14053 (redrawn from the data in Turner et al. 1971). Dashed line, whole rock; solid line, plagioclase. The discordance is strongly reduced when the phase assemblage is modified, requiring that most of the observed discordance of that sample was due not to intra-grain age gradients in a homogeneous material but rather to the simultaneous presence of young matrix (mesostasis) and old plagioclase. (**b**) Common-denominator three-isotope correlation diagram (from the data in Turner et al. 1971). Filled diamonds - unpicked whole rock; open triangles - hand-picked plagioclase. Since the Ca/K signature of pyroxene, plagioclase, and matrix is different, it is possible to assign a K-Ar age to each of these phases.

Fig. 6 - Real-color cathodoluminescence (CL) and cross-polarized light (XPL) microscopy images of feldspars in thin sections from different geologic environments. (a), (b) Sanidine crystal (blue CL) from the Peach Springs Tuff in Arizona, USA. The arrows point to the outside edge of the large previously euhedral crystal which has experienced partial dissolution but otherwise shows no evidence for metasomatic alteration by hydrothermal fluids. (c), (d) Microcline crystal from the Chain of Ponds

1077 granite (Chafe et al. 2014) in Maine, USA. The arrows point to regions in the microcline, and at the
1078 grain boundary with plagioclase (green CL), where the microcline has been partly replaced by non-
1079 luminescing adularia. (e), (f) Microcline and plagioclase from the Sweetwater Wash granite, Mojave
1080 Desert, California, USA. The bottom arrows point to regions in the microcline and plagioclase that
1081 have experienced metasomatic alteration by hydrothermal fluids. The upper arrow shows internal
1082 zoning in the plagioclase crystal that is not visible in the XPL image. The CL-revealed zoning is
1083 enriched in Ba and Sr as determined by EPMA (J.M. Hanchar, unpublished results). Mineral
1084 abbreviations: Bt, biotite; Kfs, K-feldspar; Pl, plagioclase; Qz, quartz.
1085
1086 Fig. 7 - Artificial mixtures of heterochemical, diachronous phases. (a) Age spectrum of amphibole–K-
1087 feldspar mixture (redrawn after Villa et al. 1996). Arrows indicate the ages of the pure amphibole and
1088 the pure K-feldspar. The age spectrum alone gives no clear indication on how to deconvolve the K-
1089 feldspar-dominated, artificial mixture. (b) Common-denominator, three-isotope correlation diagram
1090 (Cl/K vs Ca/K) fingerprinting the chemical signatures of the artificial mixture. Filled circles denote the
1091 pure K-feldspar (Cl-free, Ca-poor), the pure amphibole (Ca+Cl-rich), and the bulk sum of all steps
1092 (dominated by the K-feldspar). Open circles are the individual heating steps of the artificial mixture.
1093 The linear correlation (solid line) reflects the artificial binary mixing. (c) Common-denominator three-
1094 isotope correlation diagram (Ar*/K vs Ca/K). Binary mixing is shown by the solid line. By
1095 extrapolating (dashed line) the correlation to the independently determined Ca/K ratio of the pure
1096 amphibole, it is possible to successfully recover its age, even if the individual heating steps (open
1097 circles) never even approach the pure end-member. (d) Age spectra of two biotite samples and two
1098 artificial mixtures in different mass ratios (redrawn after Kula et al. 2010). Red squares - pure biotite
1099 IV8; light blue circles - pure biotite PM1; Mix1 - mixture IV8-PM1 3:1 (open brown squares); and
1100 Mix2 - mixture IV8-PM1 1:3 (open blue-green triangles). The x-axis is the step temperature (following
1101 Fitch et al. 1969), rather than the percentage release of ^{39}Ar, as it more clearly evidences the parallel

1102 differential release patterns of the two pure end-members PM1 and IV8. The age spectra alone,
1103 carrying only incomplete information, allowed Kula et al. (2010) no positive identification of the
1104 mixture's systematic behavior. (e) Common-denominator three-isotope correlation diagram relating the
1105 ages of PM1 and IV8, and the chemical signature of PM1, to those of mixtures Mix1 and Mix2
1106 provided by Kula et al. (2010). The open squares and triangles, representing Mix1 and Mix2, define an
1107 almost ideal binary mixing between PM1 and IV8. As pure biotite, IV8 had been irradiated with Cd
1108 shielding, which destroys all information regarding the Cl/K ratio. Its presumed correct position in the
1109 Cl/K-age common denominator isotope correlation diagram is shown by an open ellipse. (f)
1110 Differential Ar release plot. The release rate k on the ordinate axis is calculated from the percentage
1111 ^{39}Ar released in a given step divided by the temperature increase since the preceding step. It can be
1112 seen that the differential degassing rate of IV8 (red squares) has a different shape from that of PM1
1113 (blue circles). IV8 predominates over PM1 in two temperature intervals, i.e. $T < 700$ °C and 860 °C < T
1114 < 940 °C, in correspondence with the two age maxima of the curves labelled Mix1 and Mix2 in Figure
1115 7d. PM1 dominates the release for $T > 970$ °C, when IV8 is practically exhausted.
1116
1117 Fig. 8 - Natural mixtures of heterochemical, diachronous phases in diagenetically overprinted detrital
1118 white mica Rui9978 (diagrams redrawn after Villa et al. 2014). (a) Staircase-shaped age spectrum. (b)
1119 Common-denominator, three-isotope diagram correlating age with chemical composition. The staircase
1120 shaped age spectrum is caused by the presence of two heterochemical, diachronous phases: a Cl-poor,
1121 *ca*. 300 Ma old detrital muscovite generation, and a much younger Cl-rich metamorphic phengite
1122 over/intergrowing it.
1123
1124 Fig. 9 - Comparison of natural grain sizes of retrogression products of sheared and unsheared rocks. (a)
1125 optical microphotograph of fault rock Ga142, from the Aar shear zone (Berger et al. 2017). (b)
1126 Aluminium element map of Ga142. Magenta and red are high-Al muscovite, green and yellow are

high-Si phengite. The black circle in the middle of the picture has a diameter of 100 µm and represents an imaginary laser pit (cf. Flude et al 2014). Any 100 µm pit on this sample would include all of the mica generations at once. (c) BSE image of static retrogression of eclogitic phengite by greenschist-facies muscovite (modified after Villa 2006). Field of view ca. 40 x 80 µm. Ms3.1 stands for BSE-dark layers of replacive muscovite, with an average Si concentration of 3.1 atoms per formula unit (apfu) and an age of ca. 40 Ma. Ph3.6 stands for BSE-bright eclogitic phengite with an average Si concentration of 3.6 apfu and an age of ca. 49 Ma. Retrogression occurs in an "all-or-nothing" fashion parallel to the basal cleavage. The red circle has a diameter of 50 µm. The 100 µm pit is much larger than the entire image. The age of such a hypothetical *in situ* analysis would be 45 Ma, unrelated to both phengite formation and muscovite retrogression.

Fig. 10 - Age spectrum (solid line) of pre-heated gem-quality K-feldspar from Itrongay, Madagascar. The diffusivity of the aliquots of the present grain was studied by Wartho et al. (1999) and found to follow Fick's Law. The predicted age spectrum, corresponding to a bell-shaped core-rim age profile, and scaled by the volumes of the respective thin spherical shells of the modeled crystal, is shown by the dashed line. The nearly flat age spectrum fails to correctly extract the age zoning.

This is a preprint, the final version is subject to change, of the American Mineralogist (MSA)
Cite as Authors (Year) Title. American Mineralogist, in press.
(DOI will not work until issue is live.) DOI: http://dx.doi.org/10.2138/am-2017-6084

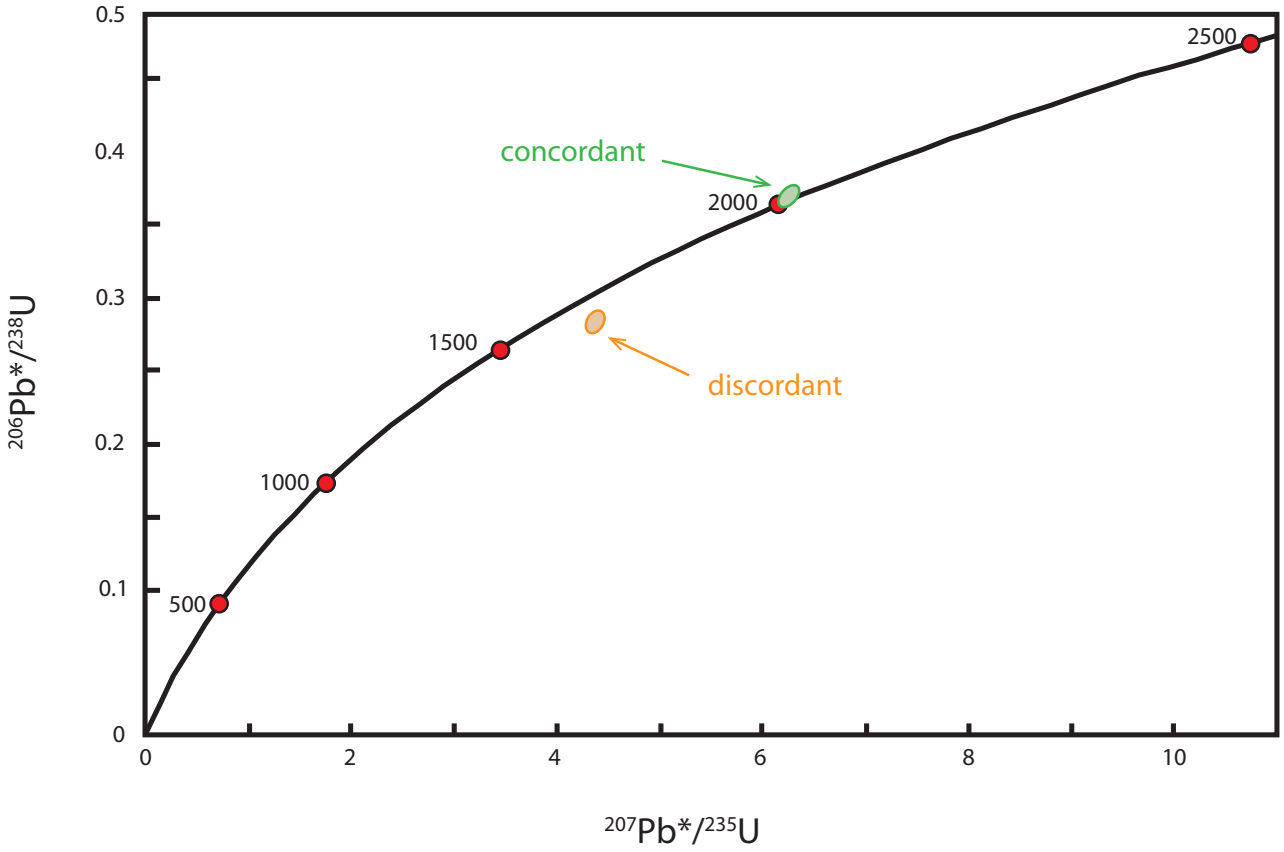

This is a preprint, the final version is subject to change, of the American Mineralogist (MSA)
Cite as Authors (Year) Title. American Mineralogist, in press.
(DOI will not work until issue is live.) DOI: http://dx.doi.org/10.2138/am-2017-6084

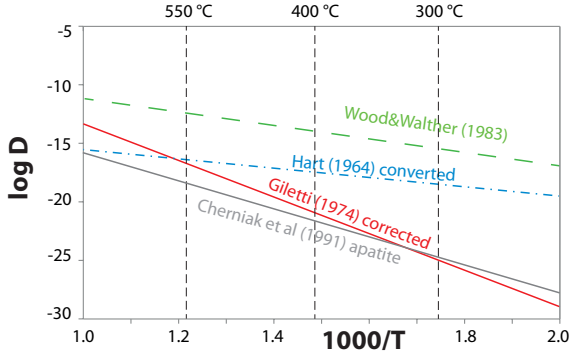

This is a preprint, the final version is subject to change, of the American Mineralogist (MSA)
Cite as Authors (Year) Title. American Mineralogist, in press.
(DOI will not work until issue is live.) DOI: http://dx.doi.org/10.2138/am-2017-6084

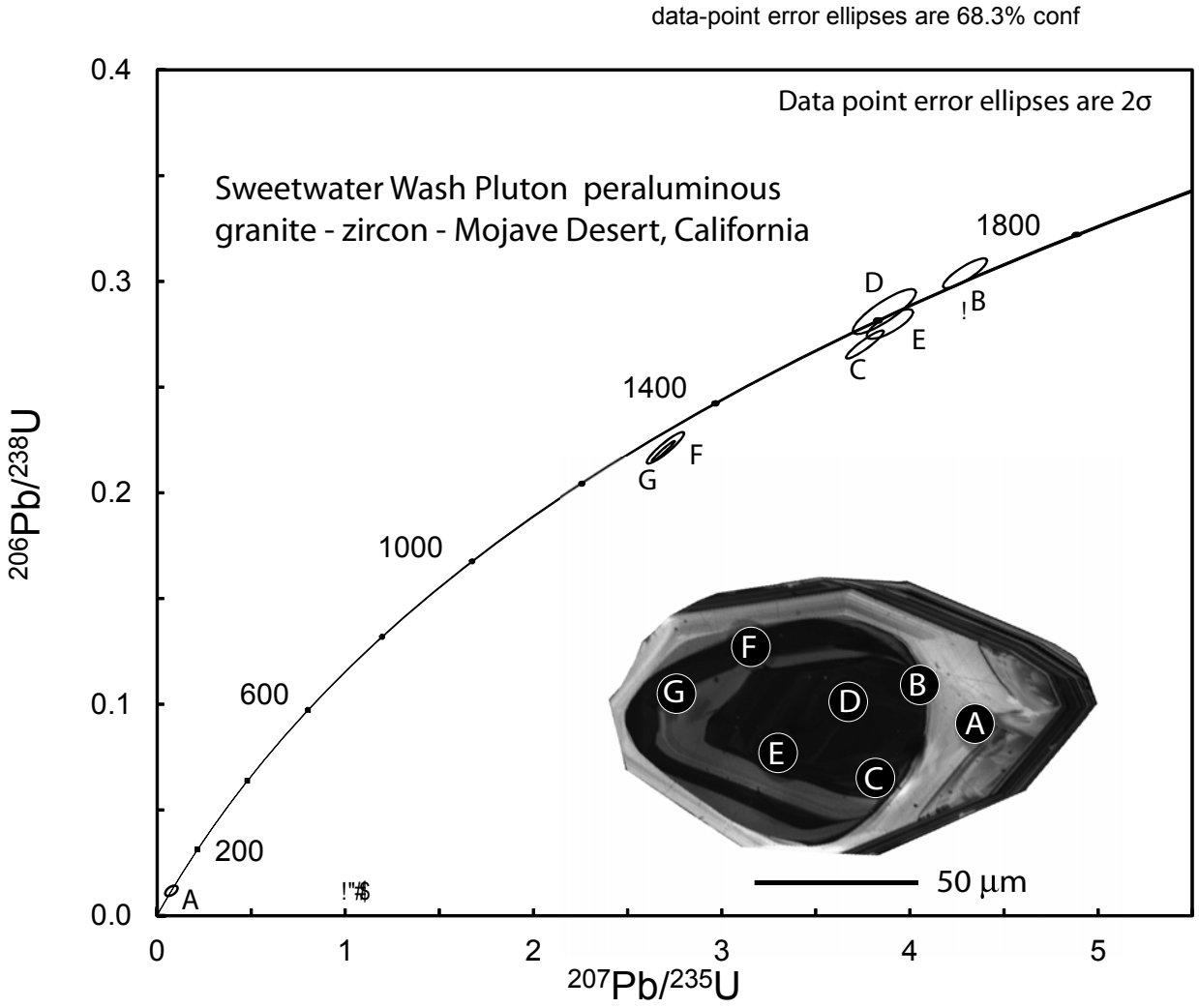

Figure 2

This is a preprint, the final version is subject to change, of the American Mineralogist (MSA)
Cite as Authors (Year) Title. American Mineralogist, in press.
(DOI will not work until issue is live.) DOI: http://dx.doi.org/10.2138/am-2017-6084

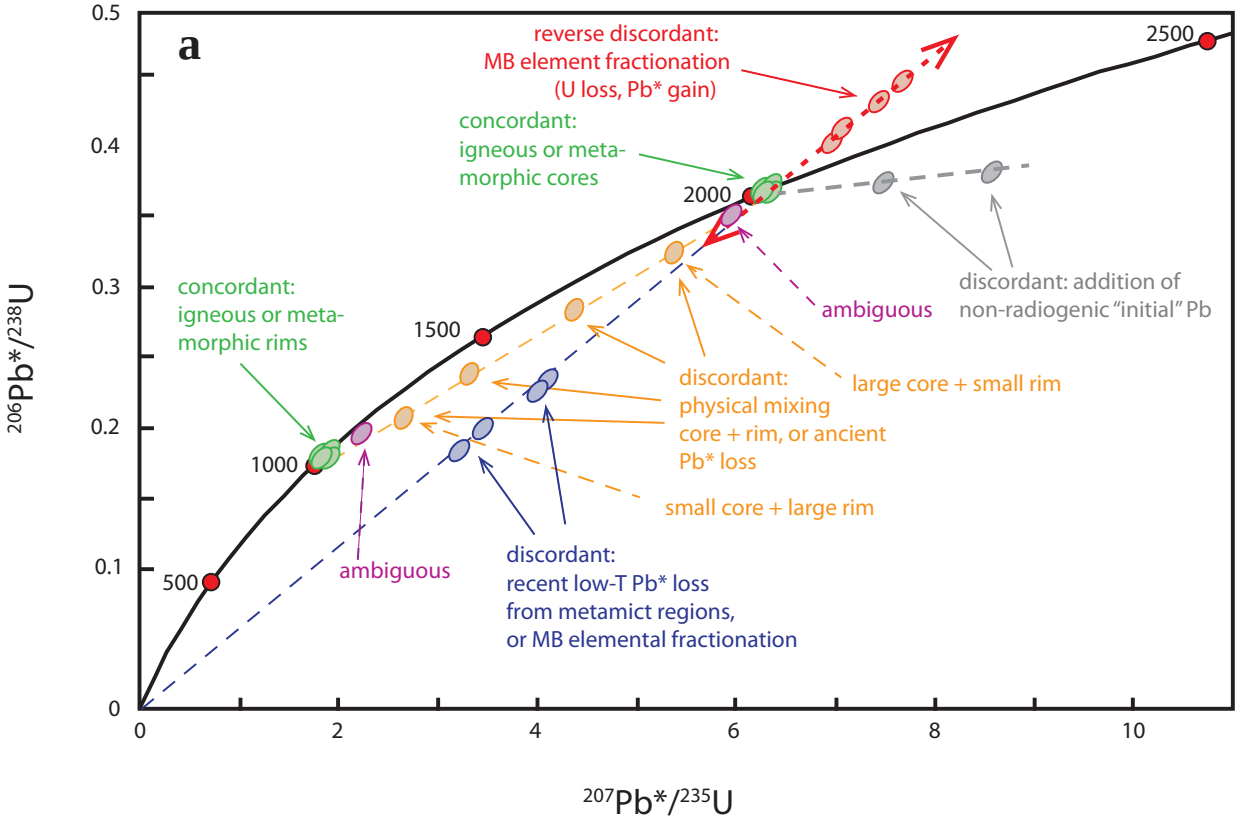

This is a preprint, the final version is subject to change, of the American Mineralogist (MSA)
Cite as Authors (Year) Title. American Mineralogist, in press.
(DOI will not work until issue is live.) DOI: http://dx.doi.org/10.2138/am-2017-6084

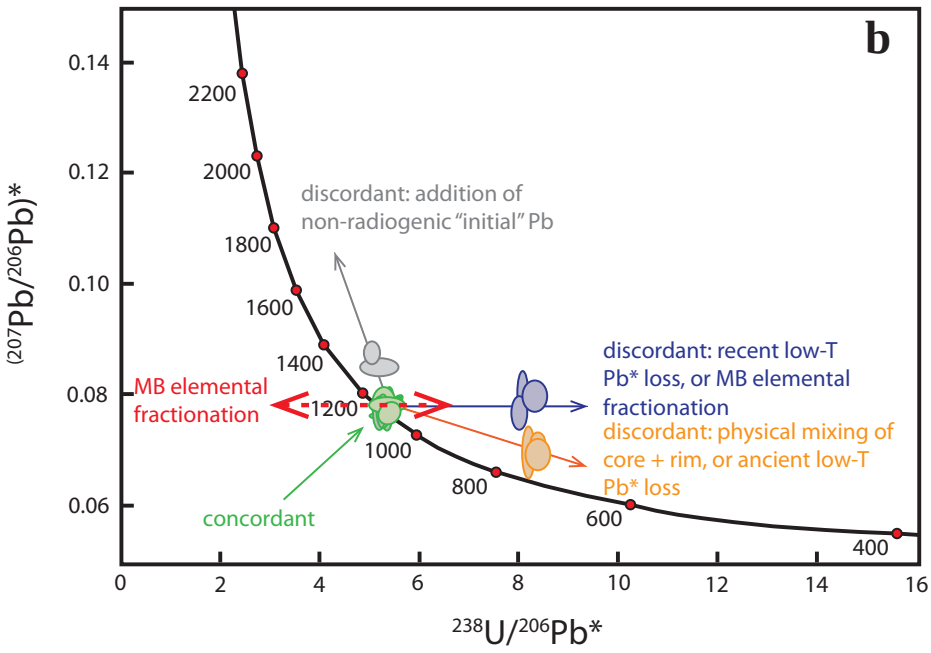

This is a preprint, the final version is subject to change, of the American Mineralogist (MSA)
Cite as Authors (Year) Title. American Mineralogist, in press.
(DOI will not work until issue is live.) DOI: http://dx.doi.org/10.2138/am-2017-6084

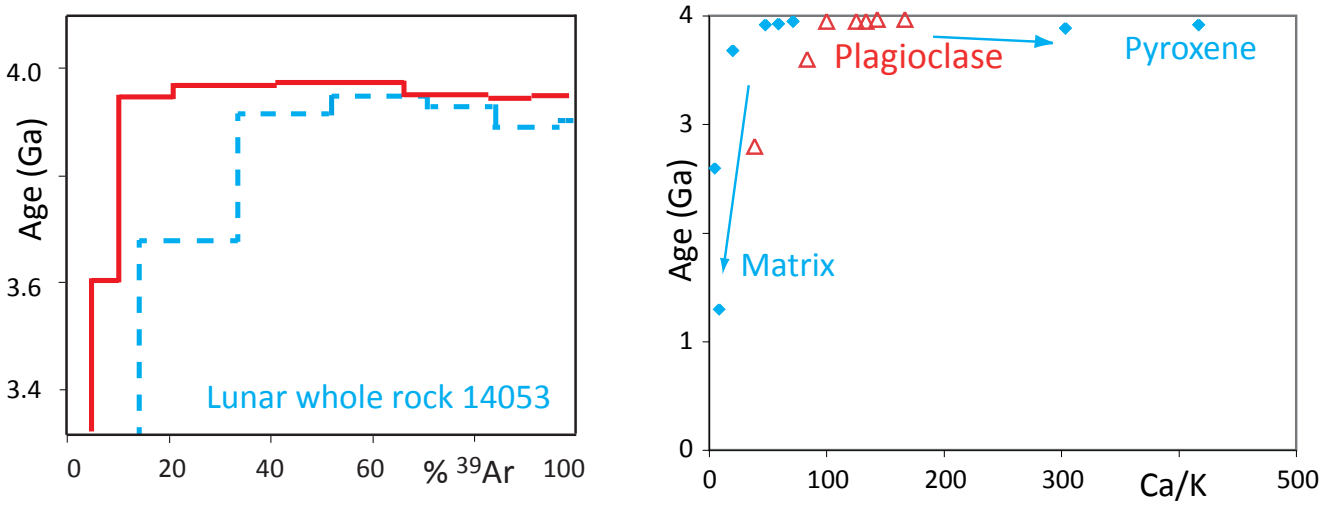

Figure 4

This is a preprint, the final version is subject to change, of the American Mineralogist (MSA)
Cite as Authors (Year) Title. American Mineralogist, in press.
(DOI will not work until issue is live.) DOI: http://dx.doi.org/10.2138/am-2017-6084

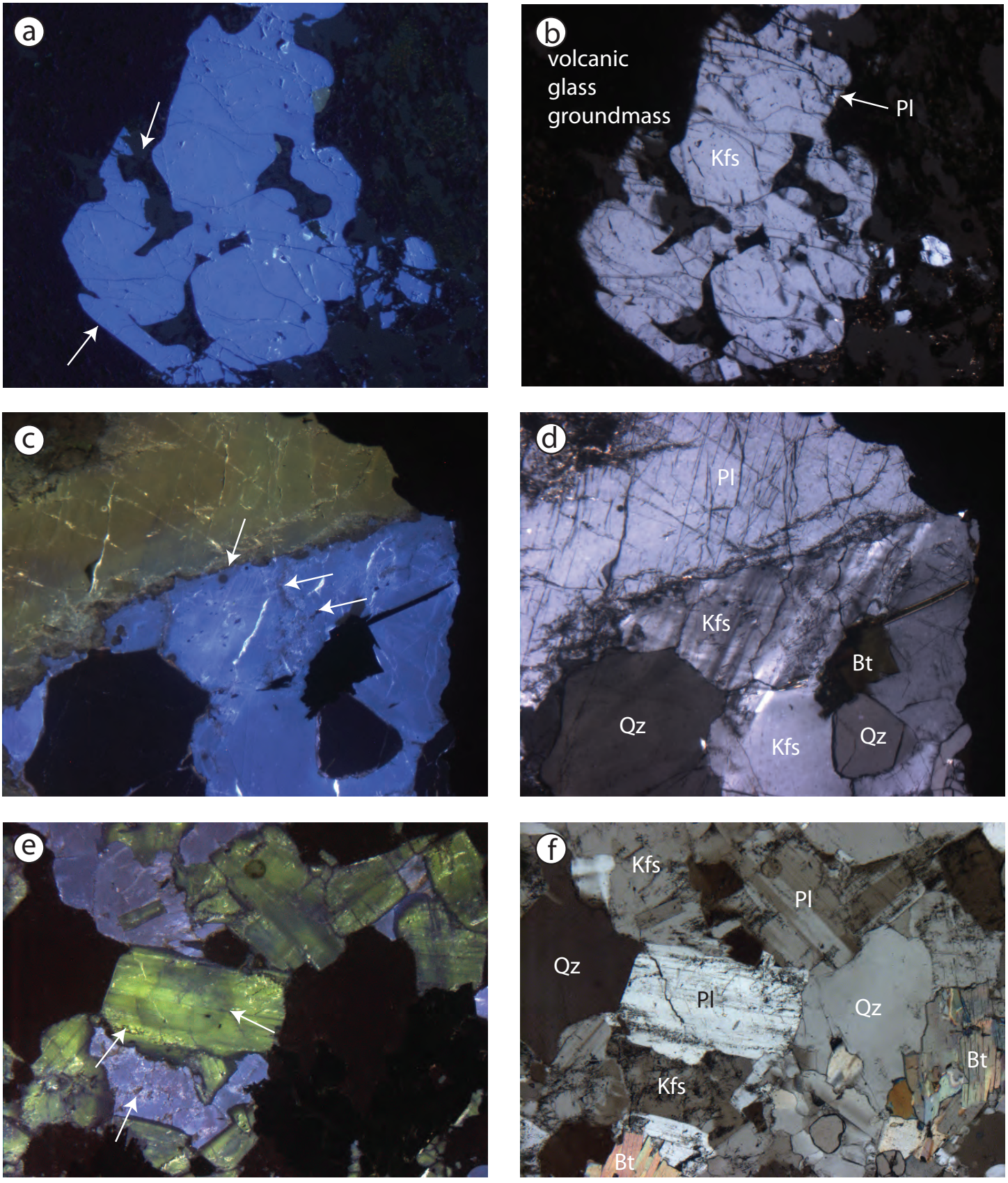

Figure 5

This is a preprint, the final version is subject to change, of the American Mineralogist (MSA)
Cite as Authors (Year) Title. American Mineralogist, in press.
(DOI will not work until issue is live.) DOI: http://dx.doi.org/10.2138/am-2017-6084

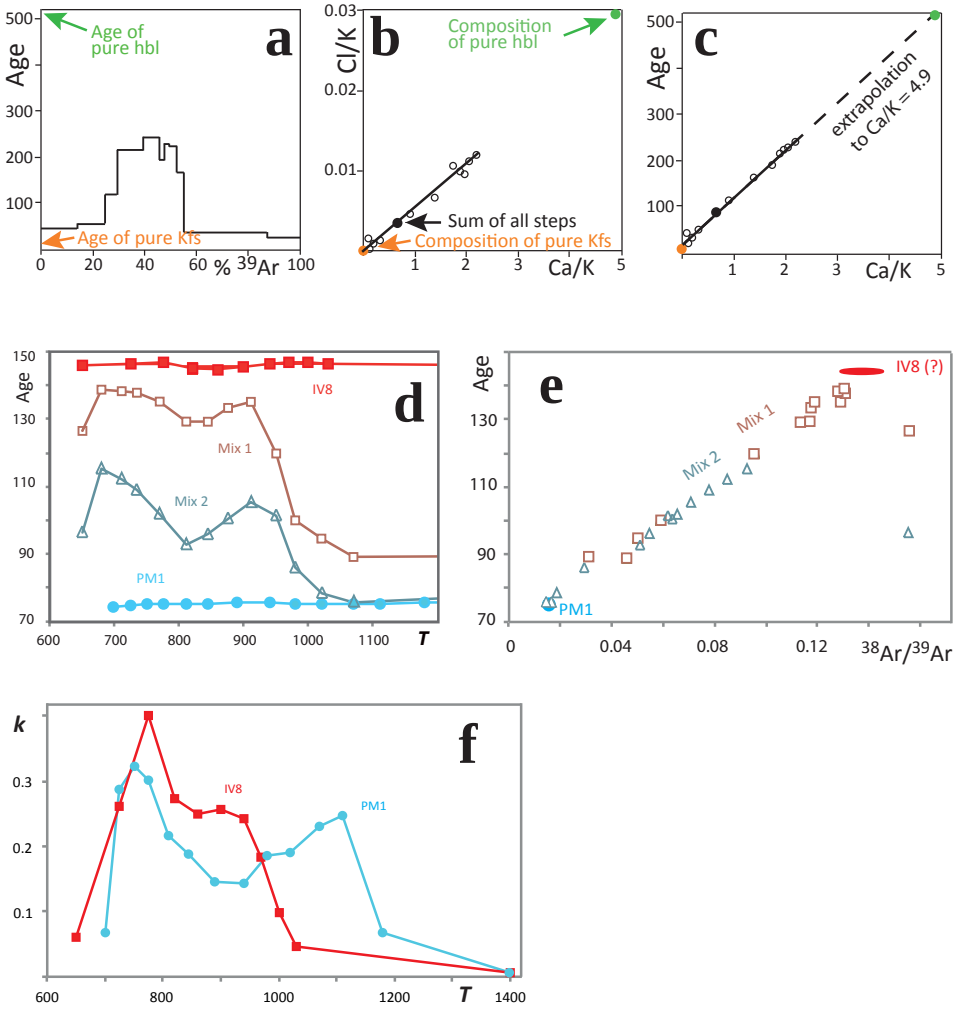

Figure 6

This is a preprint, the final version is subject to change, of the American Mineralogist (MSA)
Cite as Authors (Year) Title. American Mineralogist, in press.
(DOI will not work until issue is live.) DOI: http://dx.doi.org/10.2138/am-2017-6084

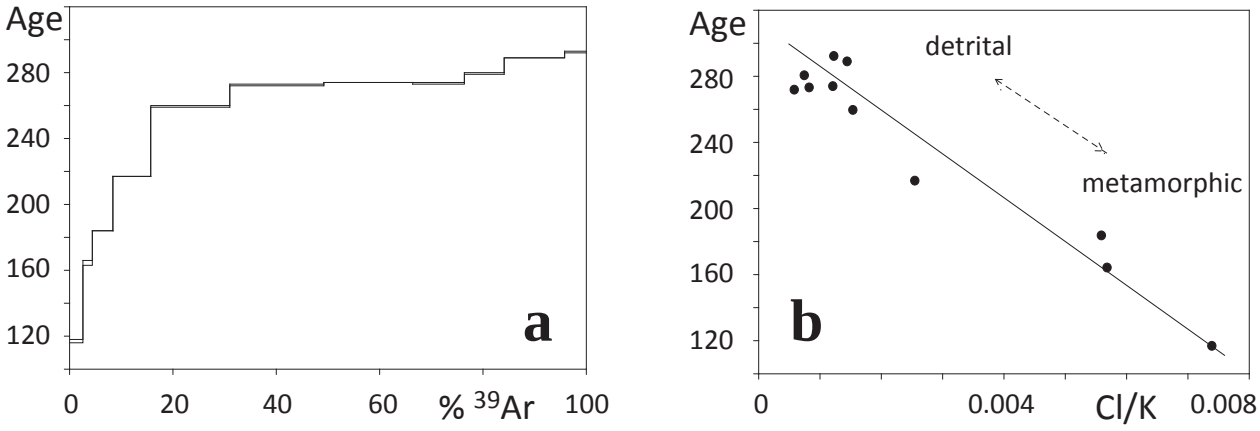

Figure 7

This is a preprint, the final version is subject to change, of the American Mineralogist (MSA)
Cite as Authors (Year) Title. American Mineralogist, in press.
(DOI will not work until issue is live.) DOI: http://dx.doi.org/10.2138/am-2017-6084

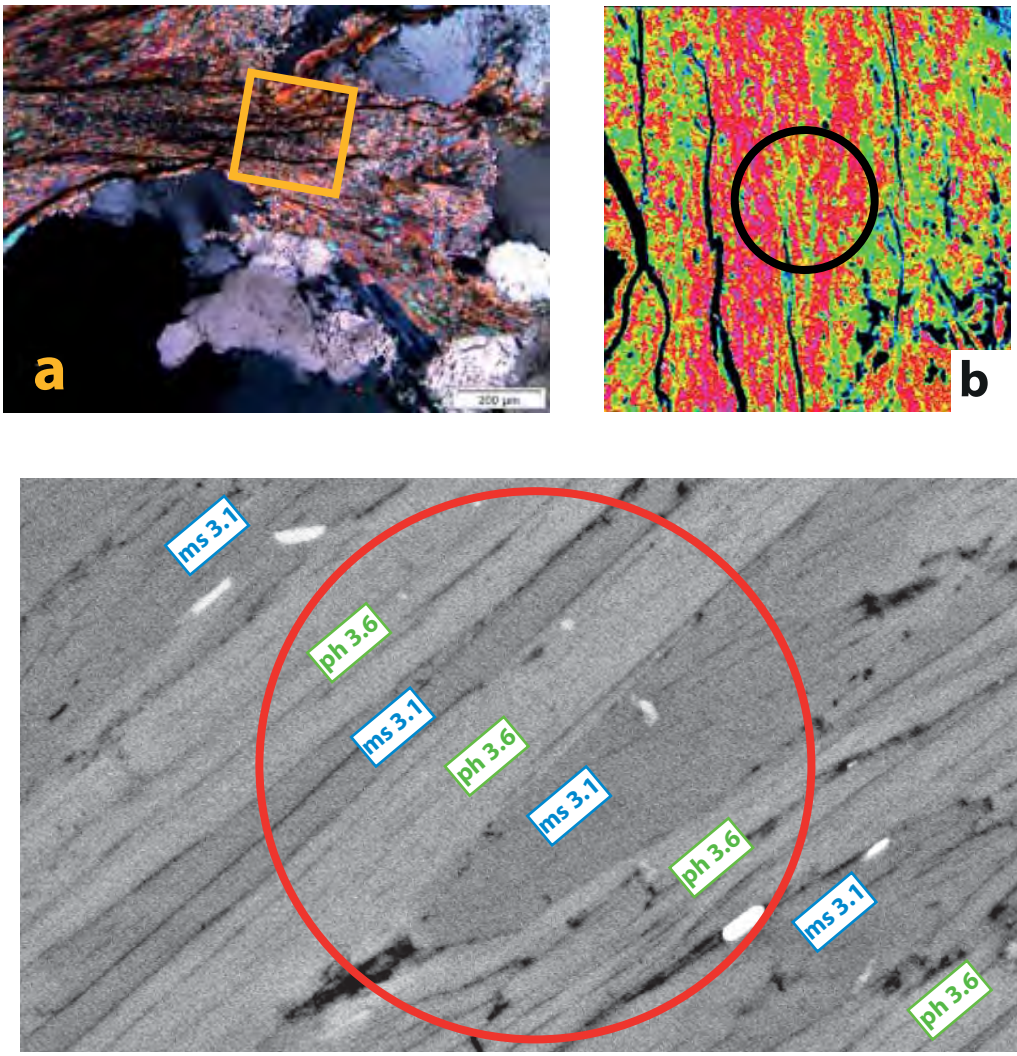

Figure 8

This is a preprint, the final version is subject to change, of the American Mineralogist (MSA)
Cite as Authors (Year) Title. American Mineralogist, in press.
(DOI will not work until issue is live.) DOI: http://dx.doi.org/10.2138/am-2017-6084